Doctoral Thesis

Synthesis and Fabrication of Graphene-Based Organic Transparent Electrodes for Flexible Optoelectronic Devices

Do Hee Lee

Department of Materials Science and Engineering

Graduate School of UNIST

2020

Synthesis and Fabrication of Graphene-Based Organic Transparent Electrodes for Flexible Optoelectronic Devices

Do Hee Lee

Department of Materials Science and Engineering

Graduate School of UNIST

Synthesis and Fabrication of Graphene-Based Organic Transparent Electrodes for Flexible Optoelectronic Devices

A thesis/dissertation
submitted to the Graduate School of UNIST
in partial fulfillment of the
requirements for the degree of
Doctor of Philosophy

Do Hee Lee

6. 8. 2020 of submission

Approved by

Advisor
Soon-Yong Kwon

Synthesis and Fabrication of Graphene-Based Organic Transparent Electrodes for Flexible Optoelectronic Devices

Do Hee Lee

This certifies that the thesis/dissertation of Do Hee Lee is approved.

6/8/2020 of submission

signature

Advisor: Soon-Yong Kwon

signature

Zonghoon Lee: Thesis Committee Member #1

signature

Myoung Hoon Song: Thesis Committee Member #2

signature

Jung-Woo Yoo: Thesis Committee Member #3

signature

Jinsung Kwak: Thesis Committee Member #4;

three signatures total in case of masters

Abstract

With the advance of electronic devices, the continued down-scaling of electronic devices has aroused the thirst for transparent electrodes (TEs) with not only excellent optoelectrical performance but also great mechanical and environmental stabilities. There are various candidates for flexible applications, such as two-dimensional (2D) materials, e.g., graphene (Gr) and transition metal dichalcogenides (TMDs) and one-dimensional (1D) materials, e.g., metal nanowire and carbon nanotube and conducting polymer. However, each candidate material has drawbacks for the use in practical applications.

A carbon-based 2D hexagonal structure, graphene has attracted lots of attention, owing to outstanding properties such as, excellent electrical and thermal conductivities, high optical transparency, gas impermeable property and great mechanical properties. However, the graphene films grown by chemical vapor deposition (CVD) are polycrystalline and synthesized on catalytic metal surfaces, leading to deterioration in its unique properties and demands for additional transfer process. As an alternative TE, there is conducting polymer. Among the conducting polymers, poly(3,4-ethylenedioxythiophene):poly(styrenesulfonate) (PEDOT:PSS) has attracted lots of attentions in organic optoelectronic devices, such as organic light-emitting diodes (OLEDs) and thin film solar cells, due to its solution processability, facile functionalization, flexibility and transparency. The organic materials, however, is vulnerable to oxygen and moisture and its acidic characteristics can damage adjacent metal layers, resulting in a degradation of the device performance.

Each representative TE material has huge drawback for the use in optoelectronics. Therefore, it is necessary to design optimal TE structures and establish proper fabrication processes for the use in next-optoelectronic applications. In this thesis, we evaluate that the potential of graphene/PEDOT:PSS organic TE composite for flexible optoelectronic devices. At first, we check the possibility for excellent optoelectrical properties, which is comparable to ITO, and compatibility of graphene/PEDOT:PSS structures via facile functionalization processes.

In addition to the property of each materials, clean interfaces is very important for formation of hybrid TE composites and conventional graphene wet transfer process should be revised because the processes hugely affect the surface quality of as-grown graphene. Based on the previous study, we devised two kinds of direct transfer strategies for the fabrication of high-quality and large-area graphene-based composite: (1) Lamination process and (2) transparent and colorless polyimide(TCPI) solution process. The direct fabrication processes without unnecessary organic layer provided excellent optoelectrical properties and better interface conditions between two heterolayers, demonstrating the relevance between optoelectrical properties and interface conditions of the TE composites. Moreover, using hall measurement and Physical Property Measurement System (PPMS), the role of graphene in graphene/functionalized PEDOT:PSS heterostructure was demonstrated in terms of electrical properties.

Furthermore, we evaluate the environmental stability of graphene-based organic TE structure under various unfavorable situations, including mechanical stress (e.g., bending and stretching) and exposure to high temperature, humidity, ultraviolet light and so on. Finally, we applied the graphene-based TE to anode for flexible polymer light-emitting diodes (PLEDs). From the harmony of each component in the TE structure, the corresponding PLEDs showed excellent performance with improved current and power efficiencies and mechanical flexibility, exceeding those of indium-tin-oxide anode-based PLEDs. These results suggest that it is important to select and design proper materials and fabrication process for hybrid transparent conducting films in practical optoelectronics.

Table of Contents

List of Figures

Photograph of our flexible PLED at radius of curvature of 2.3 mm. (f) Mechanical stability tests for flexible PLED at 5 V, with a bending radius of ~5 mm, compared to ITO-based PLEDs.

Figure 4.17. Overall device performances of Super Yellow-based PLEDs performances for different types of anode structures, in terms of representative performances: (a)Maximum luminance, (b) maximum current efficiency (CE), (c) maximum power efficiency (PE) and (d) maximum external quantum efficiency (EQE). (The average value is noted as [maximum value of performance].)

List of Tables

Chapter 1. Introduction

1.1 Transparent electrodes

Transparent electrodes, which conduct electrical current and transmit light together in visible wavelength, have been widely used in electronics such as OLEDs, OSCs, tough panel, memories and batteries.[1–3] Specifically, transparent electrodes demand high optical transmittance over 80 % at mainly 550 nm visible range and low sheet resistance below 1000 ohm per square, overcoming the trade off between optical transmittance and sheet resistance. Depending on the sheet resistance, transparent electrodes with relatively low sheet resistance less than 100 ohm per square are used in liquid crystal display, OLED and OSC. On the other hand, transparent electrodes with relatively high sheet resistance over 300 ohm per square are proper to applications of touch panel and smart windows.

Indium tin oxide (ITO), which is SnO_2-doped In_2O_3 with high band gap from 3.35 eV to 3.57 eV, has been universally used for a commercial transparent electrode, owing to its excellent optical and electrical properties.[4] However, ITO has limitation in large-area flexible optoelectronic devices, due to rareness of indium, inherent brittleness. With the gradual exhaustion of indium, indium become high-cost material. Moreover, due to its ceramic nature, ITO is brittle and susceptible to cracking under a repetitive bending. Recently, although amorphous ITO has been studied for flexible TEs, limitation in its mechanical properties and degradation of its electrical conductivity were inevitable. Therefore, development of alternative TE materials with flexibility has been ultimately demanded.

In addition to conducting part, selection of appropriate flexible substrates is another important factor for flexible TEs. In the early stages, steel use stainless (SUS) and metal foils have been also studied, however, their rough surfaces and pinhole problems limit in the use of commercial applications. Although ultra-thin flexible glass substrates with thickness of below 100 μm also have been developed for curved display application, plastic substrates, such as polyester (PES), polycarbonate (PC), polystyrene (PS), polyimide (PI), etc., have been considered as main candidates for flexible optoelectronic devices, due to their excellent inherent mechanical properties. Among them, polyimide has been widely used in flexible optoelectronics, due to its higher heat resistance over 350 °C and low coefficient of thermal expansion (CTE) below 10 ppm. However, PI has critical issues, such as the deep yellowish color characteristics with low transmittance and large anisotropy in optical properties. There are still lots of issues that should be overcome, such as minimization of thickness, establishment of low modulus, adhesion problems in organic/inorganic interfaces and so on. Moreover, in the case of polymer-based flexible applications, high permeability characteristics of plastic substrates also should be handled by designing water-impermeable layers with low permeability below 10^{-1} g cm^{-2} day^{-1}.

Therefore, a study and fabrication of appropriate transparent electrodes with excellent optoelectrical properties, mechanical and operational stabilities are very promising for the potential use in next flexible optoelectronic devices.

Figure 1.1. Applications of transparent conductive electrodes.[2]

1.2 Graphene

Since the discovery in 2004[5], graphene is a carbon-based single layer with a two-dimensional hexagonal lattice. Single crystalline monolayer graphene exhibits outstanding optoelectrical properties with a very high electron mobility up to 5×10^3 cm^2 V^{-1} s^{-1} and high transmittance of 97.7 %. Moreover, graphene also possesses good thermal conductivity (5000 W m^{-1} K^{-1})[6], excellent mechanical property with a Young's modulus of 1.0 TPa[7] and gas impermeable property[8]. Due to its unique properties, there are great expectations for graphene to be an ideal transparent electrode. However, it is still challenging to fabricate high-quality large-area single crystalline graphene without any defects and contaminants. During the preparation process of graphene, defects, wrinkles and domain boundaries are easy to occur.

Among the synthesis methods of graphene, there are top-down methods, such as mechanical exfoliation and liquid exfoliation. Mechanical exfoliation method has attracted lots of attention, due to single crystalline graphene.[5,9] However, this method is not appropriate for obtaining large-scale graphene. On the other hand, as a bottom-up synthesis, there are chemical vapor deposition (CVD) method[10,11] and Epitaxial growth on SiC[12,13]. CVD method can produce large-area monolayer graphene, however, CVD-grown graphene has relatively high sheet resistance and low mobility, owing to polycrystalline structure.[1,14] Moreover, since CVD graphene films are usually synthesized onto catalytic metal surfaces, transfer process is an essential requisite. As a transfer process, supporting layers using small organic molecules or polymers such as thermal release tape and PMMA, have been developed for fabrication process. However, their strong interactions with graphene hinder from the removal of the supporting layer, resulting in wrinkles, polymer residues and tears.[15–17] To overcome the complication of procedure, direct fabrication methods, such as roll-to-roll technique[11] and thin-film deposition processes[18,19], have been developed. However, the roll-to-roll process can result in undesirable stress to as-grown graphene, resulting in degradation such as tears and cracks.[20]

Another issue is relatively low electrical conductivity and low work function of graphene. In order to overcome the issue, several progresses on chemical doping and multilayer graphene film growth have been studied.[14,21] However, the chemical dopants, such as HNO_3[14] and $AuCl_3$[21], are very unstable in air. In addition, $AuCl_3$ dopants are easily reduced under ambient condition and results in Au particles and simultaneously aggregation of particles, resulting in rough surface and, in the case of optoelectronic devices, huge leakage current. As an alternative method, a stable doped-graphene structure using organic materials (e.g., PEDOT:PSS) has been studied, leading to higher electrical conductivity and higher work function of graphene-based structure, while maintaining high optical transparency.[22,23] However, there are still lots of difficulties in control of optoelectrical properties via additional functionalization of PEDOT:PSS and fabrication of CVD graphene-based composites. Therefore, efficient preparation strategies of CVD graphene are requisites for the use in optoelectronic devices.

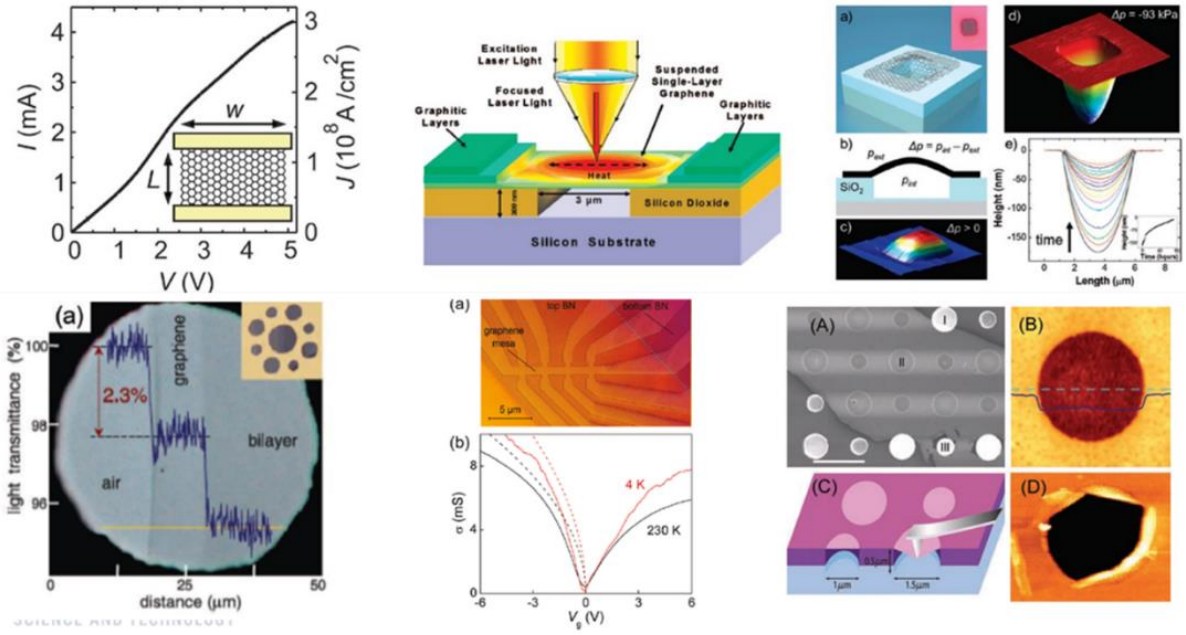

Figure 1.2. Outstanding properties of single crystalline graphene.[6–8]

1.3 Conducting polymer

Conducting polymers are organic polymers that conduct electricity. Among the conducting polymers, PEDOT:PSS has attracted lots of attentions in optoelectronic devices, such as OLEDs and thin film solar cells, due to its solution processability, high conductivity through facile functionalization, flexibility and its transparency.[22,23] PEDOT:PSS consist of positively charged PEDOT and negatively-charged PSS in the form of ionomer complex, which is combination of covalent bonds between monomers and ionic bonds between positively charged PEDOT and negatively-charged PSS. Conductive PEDOT has conjugated ring with π resonance system but it has poor dissolvability. Lot of parts in PEDOT:PSS are insulating PSS with good dissolvability. In the case of optical properties, both PEDOT and PSS are very optically transparent in the visible range. Therefore, pristine PEDOT:PSS has relatively poor electrical conductivity and good optical transparency.

In order to overcome low electrical conductivity, diverse functionalization methods of PEDOT:PSS have been developed. Most strategy is based on the expanding conducting path of PEDOT region. For example, polar solvents can induce a strong charge screening effect between positively-charged PEDOT and negatively-charged PSS. From the charge screening, the coulomb interaction between counter ions is reduced and then phase separation occurs, resulting in extension of conductive PEDOT region.[24,25] In the similar way, fluorosurfactant can induce phase separation because PEDOT and PSS have different hydrophobicity.[24] In addition, since the concentration of negatively-charged PSS is affected by acid dissociation constant of PSS, strong acid treatment also reduce the coulomb interaction between PEDOT and PSS.[26,27] In other words, facile functionalization using polar solvent, fluorosurfactant or strong acid can enhance electrical conductivity. Furthermore, since the wetting properties of PEDOT:PSS solution can be improved by fluorosurfactant, PEDOT:PSS solution treated with facile functionalization can has excellent compatibility with other transparent electrodes.

However, as an organic materials, PEDOT:PSS is vulnerable to oxygen and moisture as shown in Figure 1.4.[28] Especially, with the increase of temperature, diffusion and penetration of oxygen and moisture into organic layers are accelerated. Moreover, its acidic nature of PSS can corrode adjacent layers, including inorganic electrodes, such as ITO, and active layer in optoelectronics.[29–31] In the case of ITO/PEDOT:PSS structure, de Voigt *et al.* detected a huge amount of indium content in PEDOT:PSS films under thermal annealing and air exposure, using Rutherford backscattering spectrometry.[29] In addition to electrode parts, Baranoff *et al.* showed that iridium-based complexes also can be degraded in the presence of the acidic PEDOT:PSS layer.[30] Therefore, studying on appropriate functionalization and fabrication methods is an inevitable step for the use in optoelectronic devices.

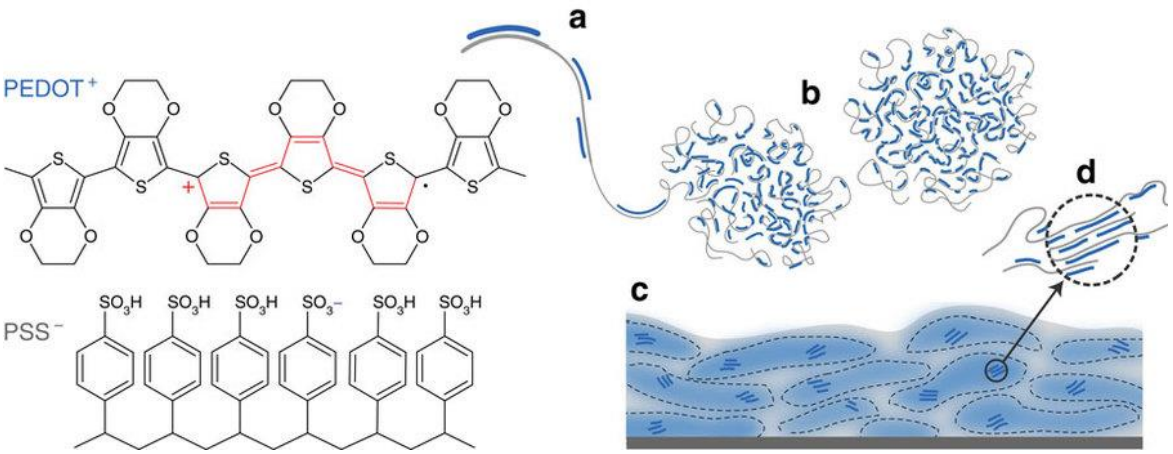

Figure 1.3. Pristine PEDOT:PSS structure and morphology.[27]

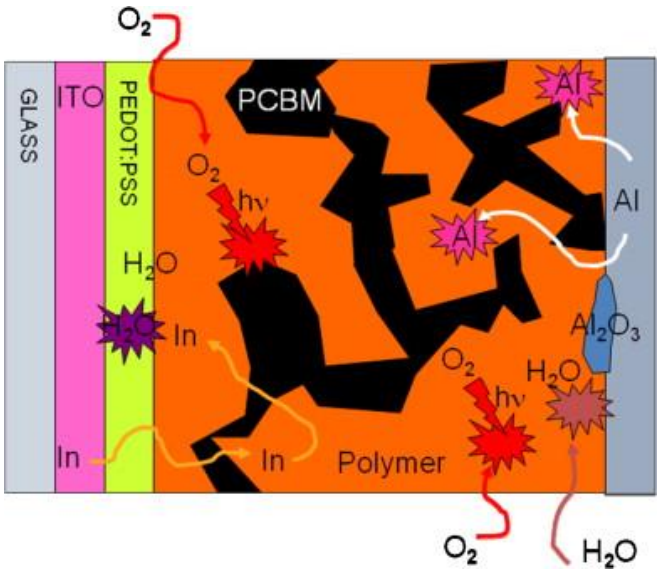

Figure 1.4. Schematic illustration of deterioration processes that occur in an organic layer.[28]

1.4 Other transparent electrodes

Among other TE materials, silver nanowires (AgNWs) and metallic nanostructures are widely studied.[32–34] AgNWs have excellent optoelectrical properties, comparable to ITO, by forming percolation of low concentration AgNWs with high aspect ratio, while offering low fabrication cost and mechanical flexibility. However, their optical haze from the scattering of light and rough surfaces limit their use in the optoelectronic devices. In order to lower a haze factor for AgNW films, fabrication methods for AgNWs with diameters around tens of nm have been developed. However, still the optical haze problem is difficult to be solved, because AgNWs dispersion contain numerous Ag nanoparticles and they are hard to separate from AgNWs, exhibiting an optical haze in AgNW films. Therefore, various studies on production and purification of AgNWs have progressed and in order to improve surface roughness and operation stability, fabrication of AgNWs-based composite has also devised for commercialization in optoelectronic devices. On the other hand, metal nanomesh has been considered as alternative TE to ITO for commercial optoelectrical applications, owing to excellent optoelectrical properties from 2~3 % of the total conducting film area, a low haze factor and mechanical flexibility. However, the large percent of insulating area can hinder from the use in the optoelectrical applications which require uniform carrier transfer on the conducting film. In addition, high optical reflectance of specific metals result in a visibility problem in tough panel. Recently, in order to overcome the drawbacks of each TE material, diverse flexible TE composites such as AgNWs/graphene, AgNWs/PEDOT:PSS, metal nanomesh/graphene and ultrastretchable TE structure using hydrogel have been developed for practical optoelectronic applications. In other words, designing and selecting appropriate electrical conducting materials and substrates is a promising research field for next-generation flexible optoelectronic devices.

Chapter 2. Synthesis of graphene and functionalization of PEDOT:PSS for high-performance transparent electrodes

2.1 Introduction

Graphene is a promising transparent electrode due to its excellent optoelectrical properties. However, although single crystalline graphene has excellent electrical properties, current CVD graphene has high sheet resistance, because CVD graphene films are polycrystalline. Another problem in use of graphene in organic optoelectronic devices is a low work function. Since organic active layers normally have high work function over 5.2 eV, there is a huge hole injection barrier between graphene and organic active layer. In order to improve the performance of graphene based optoelectronic devices, those high sheet resistance and low work function issues should be overcome.

Because of low carrier concentration of pristine graphene, chemical doping is a requirement for improvement for electrical conductivity. However, the widely studied dopants, such as $AuCl_3$ and HNO_3, are very insecure in ambient conditions.[14,21] For $AuCl_3$ doping on CVD graphene, the reduced Au particles are prone to aggregate each other, leading to rough surface and leakage current from high surface roughness in the optoelectronic devices.[35] Therefore, stable doping of graphene is one of the most critical issues for high carrier concentration.

As an alternative TE, conducting polymer, especially PEDOT:PSS has attract lot of attention in optoelectronics because its good optical transmittance in the visible wavelength and its simple functionalization can affect the optoelectrical performances, such as low sheet resistance and proper work function.[22,23] Moreover, through the control of wetting property, PEDOT:PSS can be compatible with other transparent electrodes. Due to its good compatibility, lots of research on PEDOT:PSS-based TE composites, such as graphene oxide (GO)/PEDOT:PSS, graphene/PEDOT:PSS and metal nanomaterials/PEDOT:PSS, has progressed. However, solution-processable GO/PEDOT:PSS composite has poor electrical conductivity. In the case of metal nanomaterials/PEDOT:PSS composite, the acidic nature of PSS is easy to deteriorate the metal nanomaterials, including AgNWs and ITO, especially under high temperature.[29–32] Therefore, formation of graphene/PEDOT:PSS heterostructure with good compatibility via facile functionalization of PEDOT:PSS is expected to complement each disadvantage of each material, while maintaining excellent optical transparency. In this chapter, we have studied on synthesis of graphene and functionalization of PEDOT:PSS for formation of graphene-based organic TE structures.

2.2 Experimental section

Preparation of CVD graphene

Large-area graphene was synthesized on a ultrathin Cu foil with thickness of 10 μm through the low-pressure CVD (LPCVD) system. Before graphene growth, cleaning of as-received Cu foil was sonicated using acetone and IPA and blown by N_2 gas. Then, the Cu foil was inserted in CVD quartz tube. For graphene growth, the furnace started to anneal the quartz tube till the temperature of T ≈1050 °C, while flowing H_2 gas (30 sccm). As soon as temperature approach to ~1050 °C, the pre-annealing steps for 15 min was progressed, then a CH_4(10 sccm)/H_2(30 sccm) gas mixture was injected in the LPCVD for 10 min (growth step). After the graphene growth, CVD furnace was slowly cooled down to ~700 °C, at constant flow and then cooled down to RT, rapidly.

Transfer of as-grown CVD graphene

PMMA of M_w 75,000 g/mol was prepared in toluene (4 wt%) and spin-coated onto the as-grown graphene/Cu foils at 4000 rpm for 60 s, followed by curing at 130 °C for 10 min. The growth template was dissolved by an 1 M of ammonium persulfate ($(NH_4)_2S_2O_8$). The PMMA/graphene samples were floated on DI water for 60 min and the PMMA/graphene samples were transferred onto the bare SiO_2/Si substrate. Then the sample was dried on a hot plate at ≈50 °C for 30 min and ≈120 °C for 10 min. Finally, the PMMA was removed by soaking in acetone.

Facile functionalization and preparation of PEDOT:PSS thin film

In order to functionalize PEDOT:PSS solutions, 5 wt% of DMSO and 0.05 wt% Zonyl were mixed with PEDOT:PSS solution. The mixtures filtered by 0.45 μm filters were formed as a thin film by spin-casting at the speed of 2000 rpm onto the transferred graphene on SiO_2/Si and PET substrates which was treated by O_2 plasma. Through the curing step of 20 min at 120 °C in ambient conditions, we can obtain PEDOT:PSS thin films. In order to control the thickness, we controlled the number of solution coating of multilayer PDZ films on the target substrate. The speed of spin coating was fixed at 2000 rpm, producing uniform PDZ thickness on the samples.

Characterizations

The surface morphologies of PEDOT:PSS, PDZ and PDZ-coated graphene samples were studied via an tapping mode atomic force microscope (AFM) and a field emission scanning electron microscope(FE-FEM), where the AFM model is Veeco Multimode V and a FE-SEM mode is a FEI Nanonova 230. In order to obtain Raman spectra, functionalized PDZ films were prepared on SiO_2/Si and CVD-Gr on SiO_2/Si samples. The model of Raman equipment is WiTec alpha 300R. The micro

Raman system has a excitation source of 532 nm with the laser size of ~640 nm for a ×50 objective lens with 0.9 numerical aperture, we can implement the Raman spectroscopy and mapping. The Raman data was confirmed by checking more than 10 different spots per sample. Wetting properties of bare PEDOT:PSS and functionalized PEDOT:PSS (PDZ) was measured by analyzing contact angles (Phoenix 300). Optical transmittance at 550 nm wavelength was characterized by using UV-Vis-NIR equipment. In order to determine the sheet resistance of PDZ-coated graphene films, we employed the van der Pauw method using a Lakeshore Model 642.

2.3 Results and discussion

2.3.1 Facile functionalization in PEDOT:PSS solution

In PEDOT:PSS complex, positively-charged PEDOT is a main conductive part and PSS region with negative charge is an insulating part that makes PEDOT:PSS to be hydrophilic and dissolve in solvent. Polar solvent, such as DMSO, induce the strong screening effect between counter ions. So, positively charged PEDOT can be separated from negatively charged PSS. Moreover, Zonyl which is Fluorosurfactant, enables the PEDOT which is conducting part to be more aggregated and extended. A mixture of PEDOT:PSS added with DMSO and Zonyl fluorosurfactant (designated as PDZ) was formed on substrate using spin-coating method and post-annealing. With the aggregation of PEDOT, the surface roughness increased from 1.11 nm (pristine PEDOT:PSS) to 2.10 nm (PDZ) according to the phase separation, which generated larger contact areas between the PEDOT grains.

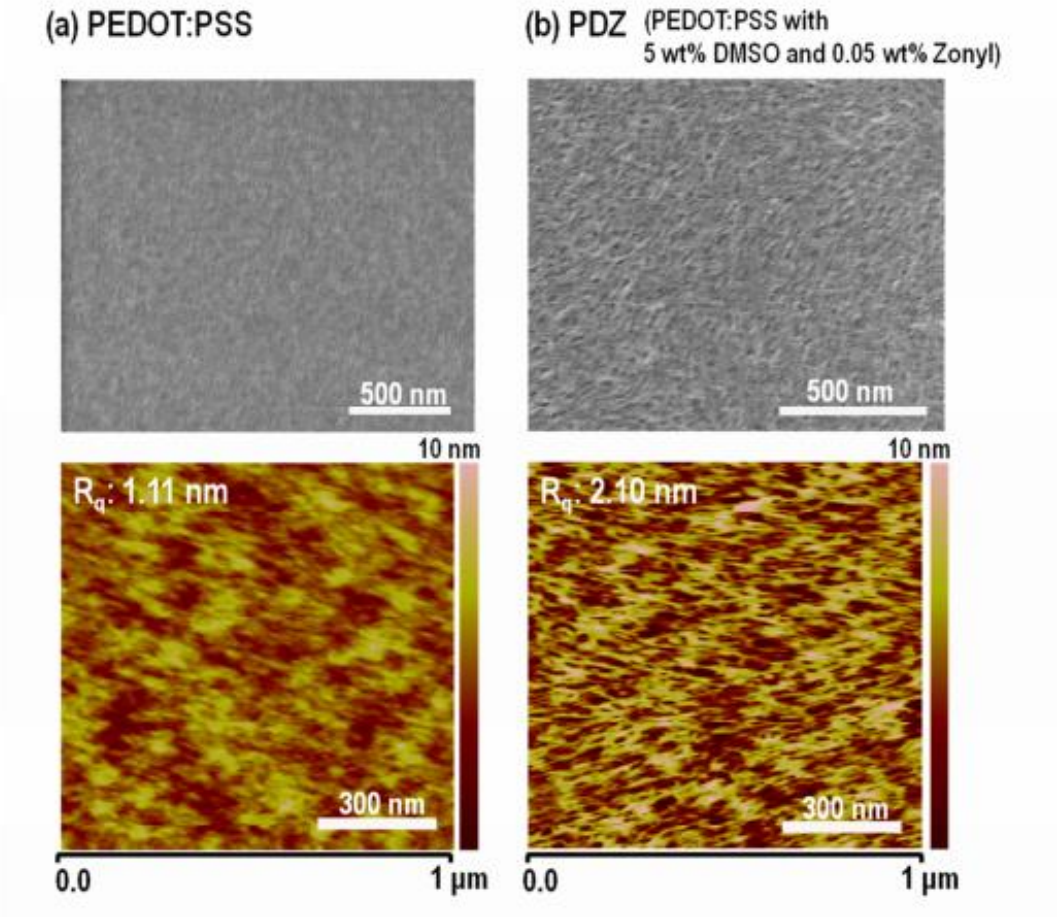

Figure 2.1. (a-b) SEM (top) and corresponding AFM (bottom) images of PEDOT:PSS films treated with different solvents according to phase-separation processes.

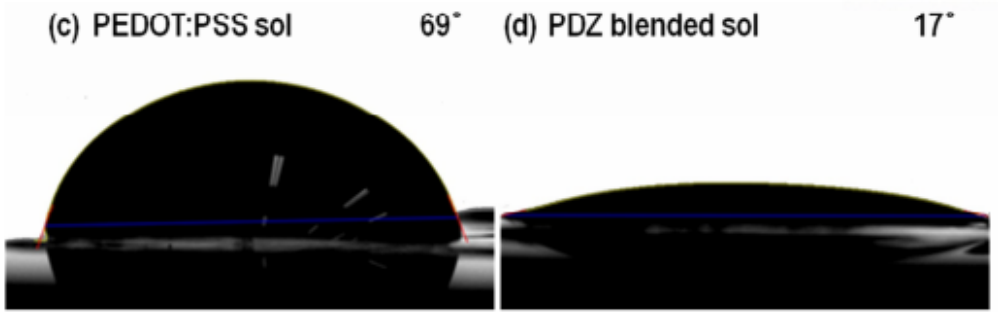

Figure 2.2. Contact angles of pristine PEDOT:PSS (contact angle ~ 69°) and functionalized PDZ (contact angle ~ 17°) on CVD-Gr.

2.3.2 Structural and optoelectrical characteristics of PDZ-coated CVD graphene

Through the functionalization and its structural change of PEDOT:PSS, the wetting properties of functionalized PEDOT:PSS was improved and the PDZ solutions were successfully coated on superhydrophobic CVD graphene. From the Raman spectra, we can check that the as-grown CVD graphene is a monolayer and in the case of PDZ-coated graphene samples, the existence of G peak (~1580 cm^{-1}) and 2D peak (~2700 cm^{-1}) of graphene under PDZ layers.

Through the doping effect PDZ on graphene, the electrical conductivity is hugely enhanced. PDZ 1L coating on CVD Gr results in low sheet resistance of ~160 ohm/sq, compared to ~500 ohm/sq of as-grown CVD graphene. Moreover, through a control of PDZ thickness, the GL-TE film can achieve the good electrical properties. The sheet resistance of PDZ/Gr can be measured depending on the number of PDZ coating, through van der Pauw method. As the number of PDZ coating increases, the sheet resistance of PDZ/Gr is hugely reduced from 160 ohm/sq (1L) to 48 ohm/sq (4L). On the other hand, optical transmittance has the opposite tendency to sheet resistance, with the increase of layer thickness. Through optimization of PDZ thickness, at the second PDZ coating cycle, we can achieve organic transparent electrodes with excellent optoelectrical properties of a sheet resistance of 86.4 ohm/sq with a transmittance of 91.0 % at 550 nm, comparable to other conductive organic-based TEs.[36–38]

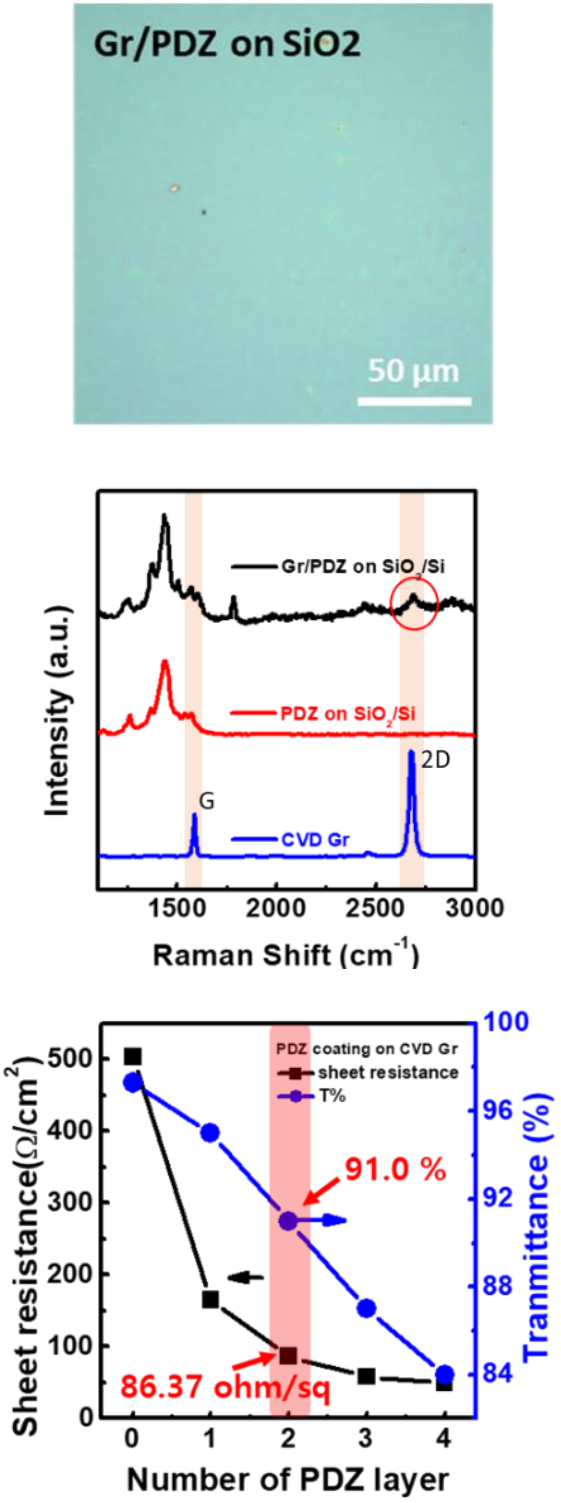

Figure 2.3. Structural characteristics of PDZ-coated graphene on SiO_2/Si substrates. Raman spectra of PDZ-coated graphene SiO_2/Si (black line), PDZ film on SiO_2/Si (red line) and as-grown CVD graphene on SiO_2/Si (blue line). Sheet resistance and Transmittance of PDZ-coated graphene samples as a function of the number of PDZ layers.

2.4 Summary and Outlook

In this chapter, through the doping strategy of CVD graphene through facile functionalization of PEDOT:PSS, we can check the potential of graphene/PDZ hybrid structure in an alternative TE material, compared to ITO. Through charge screening effect of DMSO and addition of Zonyl fluorosurfactant, pristine PEDOT:PSS with low conductivity and poor wetting properties is greatly improved, exhibiting low sheet resistance of 120 ohm/sq with high transmittance of ~90 % at 550 nm wavelength. Also, due to improvement of hydrophobic properties of PEDOT:PSS and its good compatibility, the PDZ solution is uniformly spin-coated onto as-grown CVD graphene. Through optimization of the number of PDZ coating cycles, PDZ-coated CVD graphene can obtain a sheet resistance of 86.4 ohm/sq with a transmittance of 91.0 % at 550 nm, which is comparable to conventional ITO electrodes. However, compared to metal-based electrodes, electrical conductivity should be improved through further study on functionalization of PDZ layer and proper fabrication method of PDZ/Gr structure should be developed for better optoelectrical properties of the organic TEs, exceeding the performance of ITO electrodes and clean interface between CVD graphene and PDZ layers. Therefore, in the next step, we devised simple direct fabrication process of the graphene/PDZ heterostructure via simple lamination process without using unnecessary supporting layers. Through additional studies on optoelectrical characteristics and operational stability tests of the fabricated graphene/PDZ structure, we evaluate the capability in the use for PLED devices.

Chapter 3. Fabrication of graphene/PEDOT:PSS composite on various plastic substrates thorough lamination process

3.1 Introduction

New various flexible TE materials have been developed, including 2D materials of graphene, transition metal dichalcogenides (TMDs) and metal nanomesh and 1D materials of AgNWs and carbon nanotubes (CNTs).[1,39–43] Recently, CVD graphene have been considered as "an ideal flexible TE material" due to its unique characteristics such as high electrical and thermal conductivities, flexibility, bendability or even stretchability. However, the use of graphene as practical TEs has been limited by the lack of large-area fabrication technique on organic substrates.[1] As an alternative TE, conductive polymers also have only been used for organic optoelectronics, particularly such as OLEDs and OSCs, due to their structural characteristics and facile functionalization. Tuning properties of organic compounds through chemical deformation can be utilized to enhance device performance in the points of charge separation, light absorption and transportation.[40] Conductive polymer has been considered as being potential for practical optoelectronics due to a low-cost solution process, flexibility, transparency and low weight, enabling small print-based fabrication and large-scale roll-to-roll fabrication. However, the ultimate test for commercialization is the performance and environmental stability of each layer. Since the organic compounds are fragile to several environmental factors, including exposure to moisture and ultraviolet (UV) light, and mechanical and thermal stresses, observation on the fragility of organic compounds can highlight the structural advantages that protects from those unfavorable agents.

Extensive progress has been developed to handle with the transfer problem of CVD-grown graphene (CVD-Gr). Since general CVD-grown 2D materials are grown on growth substrate such as Cu(or Ni) foil, the transfer process of as-grown CVD Gr is indispensable. Lots of study on the supporting materials, such as organic molecules and polymers (e.g., thermal release tape and PMMA) have been studied for fabrication of CVD graphene-based applications. However, those supporting layer is difficult to be removed because of the strong interaction with graphene. Especially, conventional PMMA transfer method results in interfacial perturbations, such as wrinkles, tears, polymer residues and voids. This damage affects optoelectronic performances and deteriorates the interface properties, leading to formation of tears, wrinkles and rough surfaces in thin-film devices such as PLED and OSC.[41–43] Therefore, in order to improve high-performance graphene-based optoelectronic devices, proper transfer methods are demanded.

In this chapter, based on the former study on facile functionalization of PEODT:PSS and PDZ/Gr hybrid TE structures, we devised new fabrication method of graphene-based hybrid TE structure, using lamination process. Lamination process enables as-grown CVD graphene to be directly transferred onto desired substrate, such as glass, polyethylene terephthalate (PET), urethane, PDMS and so on, uniformly and conformally. Without any unnecessary PMMA supporting layer or other perturbations, clean interface in Gr/PDZ films can be formed and lowers the contact resistance between graphene and PDZ layers. Moreover, the optoelectrical performance of Gr/PDZ films can be optimized by controlling PDZ thickness. Furthermore, for operational stability tests, the Gr/PDZ samples were evaluated under unfavorable environments, such as mechanical and thermal stress, high temperature and high humidity. By demonstrating environmentally stable and highly conductive Gr-based organic TEs, our work can pave the way for next flexible optoelectronic devices.

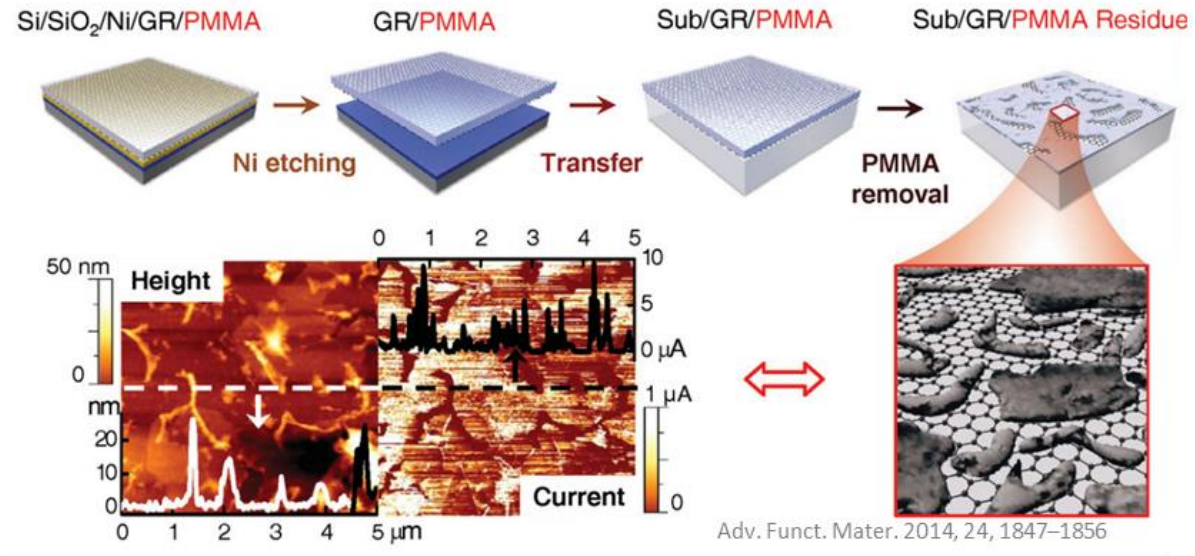

Figure 3.1. Schematic of conventional PMMA-assisted transfer process for CVD graphene.[23]

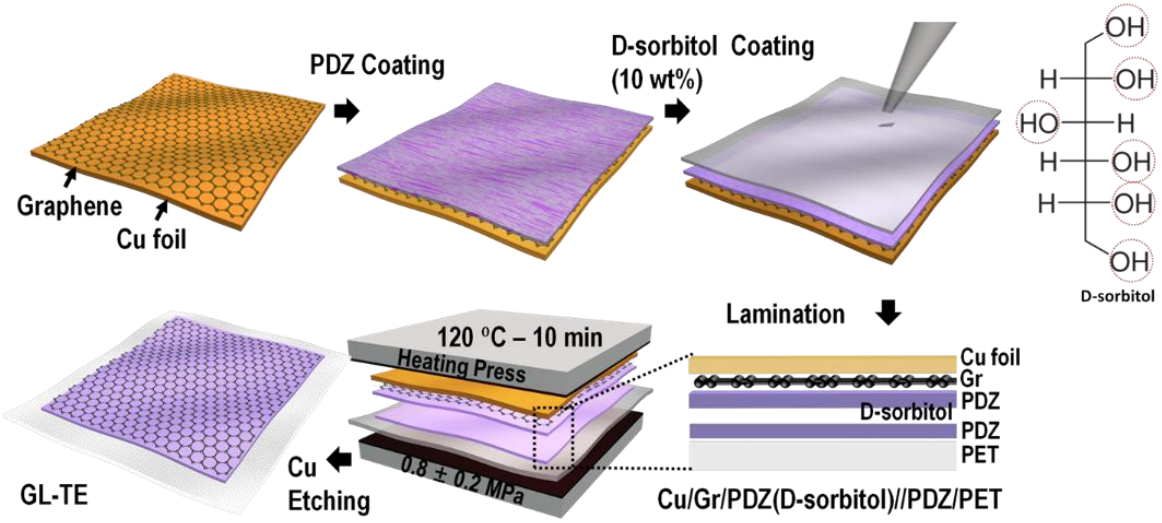

Figure 3.2. Schematic of direct transfer process for CVD graphene, using lamination process.

3.2 Experimental section

Preparation of CVD graphene

Synthesis conditions of CVD graphene are same with the previous procedure in 2.2 Experimental section. Furthermore, we check that there is a relevance between foil thickness and the amplitude of rolling features in the Cu foil because the surface morphology of the GL-TE samples resembles the one of the foils. Since the Cu foils have rolling feature with large roughness, we analyze two kinds of Cu foils with different thickness 10 μm and 25 μm for the area of 2500 μm^2, via AFM. In the case of each 25 μm and 10 μm thick Cu foil sample, the surface roughness was ≈208 and 95 nm, respectively. In the case of Cu foils with thickness below 10 μm, better surface morphology was observed, however, there is a difficulty in handling. Therefore, we chose a Cu foil with thickness of 10 μm for a graphene grow template.

Lamination Process

PDZ solution is prepared in the same way, as written in the previous procedure in 2.2 Experimental section. The mixtures filtered by filters with 0.45 μm pore size, were formed on Gr/Cu foils and O_2 plasma-treated PET substrates by spin-coating of 2000 rpm, cured by 120 °C annealing process of 20 min in the ambient condition. In order to control the thickness, we controlled the number of solution coating of multilayer PDZ films on the target substrate. Then, PDZ solution added with 20 wt% D-sorbitol for adhesive property was treated on the Gr/Cu foils. Through annealing process above100 °C, the D-sorbitol could act as a transparent glue at a lamination step, while maintaining high optical transparency. As soon as PDZ/Gr/Cu and PDZ/PET were prepared, we applied heat of ~120 °C and simultaneously an small amount of pressure with ~0.8 ± 0.2 MPa and for 10 min, using a heating pressure. After the Cu foils were rinsed by 1 M of $(NH_4)_2S_2O_8$ solution and DI water, the Gr/PDZ/PET assembly, which is designated as GL-TE, was successfully formed.

Characterization

The surface morphologies of PEDOT:PSS, PDZ and PDZ-coated graphene samples were studied via an tapping mode atomic force microscope (AFM) and a field emission scanning electron microscope(FE-FEM), where the AFM model is Veeco Multimode V and a FE-SEM mode is a FEI Nanonova 230. The model of Raman equipment is WiTec alpha 300R. Using the micro Raman system has a excitation source of 532 nm with the laser size of ~640 nm for a ×50 objective lens with 0.9 numerical aperture, we can implement the Raman spectroscopy and mapping. A spectroscopic image of Raman mapping was obtained by measuring the Raman spectra of each individual pixel around the 2D peak of graphene, with a 70 μm × 70 μm area. The Raman data was confirmed by checking more than

10 different spots per sample. In order to characterize the physical properties of TE samples such as mobility, carrier concentration, I–V curves, Hall voltage, Hall coefficient, resistance and resistivity, Hall measurement was implemented, using a Lakeshore Model 642 electromagnet. For analysis of Hall measurements, four contact pads in Au/Cr electrodes (35 nm/5 nm) of 1 cm × 1 cm size via e-beam evaporation were deposited onto the samples. In the case of Hall measurement, contacts were exposed to perpendicular magnetic field B from which the lateral or for the Hall coefficient, hall resistance R_{xy} was extracted, $R_H = R_{xy}/B$, in the range from 1.0 kG to 10.0 kG, where the step size was 1.0 kG. We implement the variable field measurement according to linear sweep from positive field to negative field. Similarly, carrier density was inversely proportional to hall voltage, $V_H = R_H I_x B_z/t$, where $|R_H| = 1/pe$, B_z is the perpendicular applied magnetic field, I_x is transverse current fixed at 1 nA, e is the electronic charge, p is the concentration of the charge carriers and t is the thickness. Calculation of $\mu = \sigma|R_H|$, provided us the estimated Hall mobility, in terms of thickness and the sheet resistivity of the samples.

CTLM Method: The well-known transmission-line matrix (TLM) method has been widely used to evaluate sheet resistances and contact resistances in the interfaces. However, traditional linear TLM techniques tend to go through the current crowding effect and two lithographic steps are required to process TLM patterns. To overcome this drawback, we introduced circular TLM (CTLM) method, because CTLM does not demand an additional procedure for etching and the current confinement perpendicular to the contact is measured. For CTLM measurement, circular contacts kept the distance with outer contact with different spacing of 10, 20, 40, 80, 160, 320, 640, and 1,280 μm, to the inner contact (100 μm), were patterned through a photolithography process. Then, as an electrode pad, 5nm-thick Cr and 35nm-thick Au was deposited by e-beam evaporator. The estimated nonlinear curve from the CTLM data can be converted into a linear relevance between the gap interval and the total resistance by considering the correction factors. The transfer length (L_T) and R_S of conducive layer can be measured by the well-known equation for CTLM, $R_T = (R_S/2\pi)\{\ln(1 + S/r_I) + L_T(1/r_I + 1/(r_I + S))\}$,[42,43] where r_I is the inner contact radius, R_T is the total resistance between the outer and inner contacts and S is spacing of the contact pad.

Ultraviolet photoelectron spectroscopy (UPS): UPS analysis was implemented for investigation of the work functions of the samples. UPS equipment is an Axis-NOVA model (Kratos. Inc.). Base pressure was 10^{-7} Pa. A pass energy is 1.0 eV at 0.05 eV per step and the non-monochromatic radiation of He I (21.2 eV) was used. An atomically clean Au help to measure the energy calibration and ensure accurate values for Fermi edge before measurement, while applying −15 V bias for enhancement in the secondary photoelectron cut-off. UPS measurements was implemented to measure the work function of samples, which can be measured from $\phi_\upsilon = h\upsilon - |E_{cutoff} - E_{FE}|$, where, for He I source, $h\upsilon = 21.2$ eV, where E_{FE} is

the Fermi edge and E_{cutoff} is the onset of secondary emission cut-off edge.

X-ray photoelectron spectroscopy (XPS): The surface composition and chemical structure of the samples were inspected through XPS analysis. For XPS equipment, 72 W-power aluminum K_α non-monochromatic X-ray excitation was equipped and an analysis diameter was ~0.4 mm and a pass energy was 50 eV. The XPS analysis was implemented on a K-alpha spectrometer (Thermo Fisher) for the electron analysis. ~1×10^{-9} mbar of the chamber base pressure was maintained.

Humidity Stability Tests and UV Light Irradiation: In the case of high relative humidity stability tests, high relative humidity environment was set up in a homemade chamber. The humidity was controlled by bubbling dry N_2 gas. In order to evaluate the electrical stability under exposure to the UV light, a light of UV lamp, which is VL-6.LC in Vilber Lourmat, with a 6 W with an emission wavelength of 254 nm, was applied to test samples in the dark. During both stability tests, the resistance of the samples was measured as a function of time at a constant applied voltage of 1 V (Keithley 2636A).

Thermal Stability: We implemented operational stability under thermal stress by evaluating change in the sheet resistances of the samples as a function of temperatures between 25 and 210 °C using the four-probe station with a function of hot plate applied by an source meter of Agilent B1500A.

TGA Measurements: TGA analysis was implemented via a TA Instruments Q500 analysis equipment in terms of four different heating rate (1, 2, 5, and 10 °C min^{-1}) under a N_2 ambient condition. The range of temperature in TGA was from 50 to 700 °C at a constant flow rate of N_2 at 60 mL/min. All samples were evaluated at reduction in the weight of ~10 wt%. In the TGA approach, the material is heated along different thermal curves. The first step in the data analysis process is the choice of a constant decomposition level, which is defined from the resulting thermal curves. As shown in Figure 3.3, the profile corresponding to 20% weight loss (conversion) is used in the following calculations as a failure criterion because a value early in the decomposition profile of PEDOT:PSS below about 250 °C is involved in volatilization processes, such as removal of moisture. A plot of the logarithm of the ramping rate versus the reciprocal the temperature at a constant decomposition level provided the activation energy. $E = -R/b[dlog\beta/d(1/T)]$, where E is activation energy for thermal degradation (J/mol), R is gas constant (8.314 J/mol K), T is temperature at constant conversion (K), β is a heating rate (°C min^{-1}) and b is a constant. The value of the constant b can change depending on the value of E/RT. By inputting b into initial value of 0.457, an iterative process results in E and b with new value, until E no longer changes with continual iterations. This obtained activation energy is then used to determine the estimated lifetime at a chosen temperature.

Estimation of device lifetime under thermal stress: Derek J. Toop proposed a relation between TGA

theory and the lifetime of polymers (thermal stability under isothermal conditions). In Figure 3.5, from Toop's relation, the estimated time to failure, t_f can be calculated by inputting the previously obtained parameters of the activation energy E, constant b and the constant failure temperature T_f. By calculating the estimated time for several failure temperatures, a graph of the estimated life as a function of the corresponding reciprocal temperature for 20 wt% loss was obtained. From this graph, we can easily deduce the lifetime of a Gr-laminated film until failure (20 wt% loss) at any constant temperature. $ln\ t_f = E/RT_f + ln[E/\beta R \times P(X_f)]$, where t_f is an estimated time to failure (min), T_f is a failure temperature (K), $P(X_f)$ is a function whose values depend on E at the failure temperature and T_c is a temperature for 20 wt% loss at b (K).

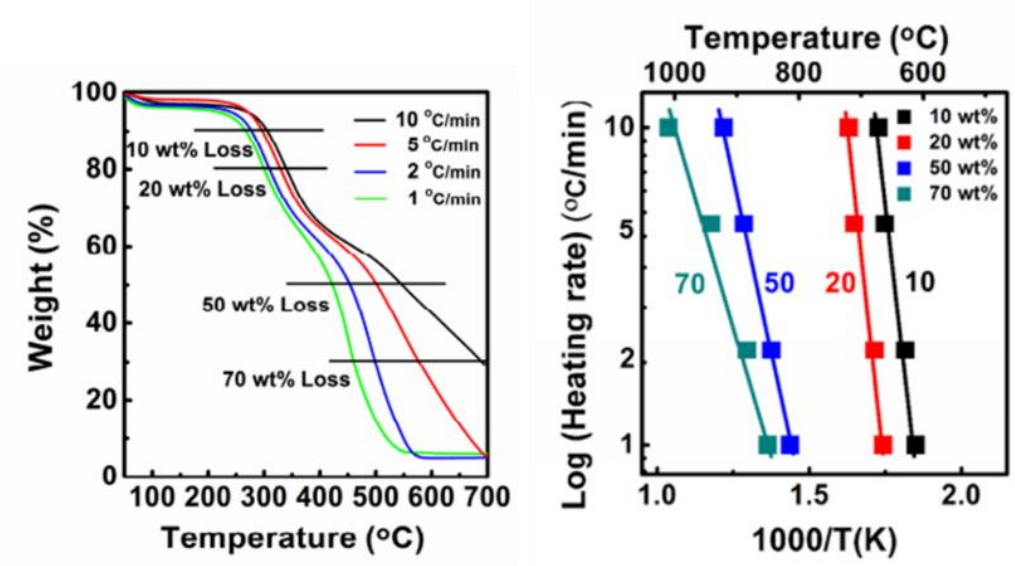

Figure 3.3. TGA weight loss curves of GL-TE films at different ramping rates of 1, 2, 5 and 10 °C/min and transformed logarithm of the heating rate vs. the reciprocal of the temperature at different constant conversion levels.

$$E = \frac{-R}{b}\left[\frac{d\log\beta}{d(1/T)}\right]$$

where:

E = Activation energy (J/mol)
R = Gas constant (8.314 J/mol K)
T = Temperature at constant conversion (K)
β = Heating rate (°C/min)
b = Constant (Initial value: 0.457)

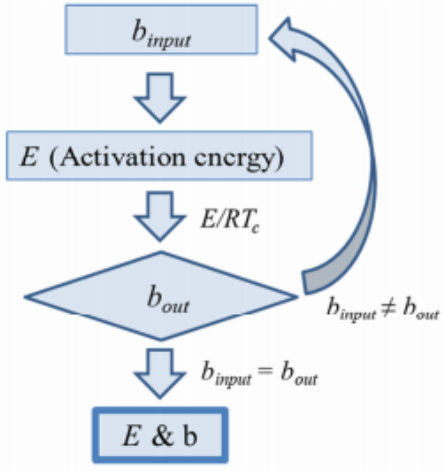

Figure 3.4. Calculation of the activation energy (E) from the slope of the lines in figure x, using the method of Flynn and Wall (iteration method).

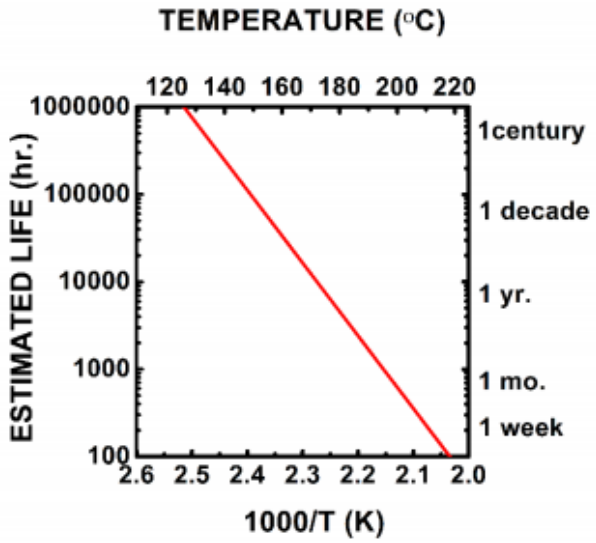

$$lnt_f = \frac{E}{RT_f} + ln\left[\frac{E}{\beta R} \bullet P(X_f)\right]$$

where:

t_f = Estimated time to failure (min)
T_f = Failure temperature (K)
$P(X_f)$ = A function whose values depend on E at the failure temperature.
T_c = Temperature for 20 wt% loss at b (K)

Figure 3.5. Estimated lifetime of GL-TE film as a function of failure temperature.

3.3 Results and discussion

3.3.1 Structural characteristics of graphene-laminated transparent electrodes

Figure 3.6a shows a photograph of the 2.5 cm × 2.5 cm as-synthesized GL-TE film sample through lamination process. Figure 3.6b–d shows the typical structural characteristics by observing surface morphology and Raman spectra of samples. OM and Raman mapping demonstrated that graphene/PDZ hybrid structure was successfully and uniformly fabricated on PET substrate. As shown in Figure 3.6b, the morphologies in OM data resemble those of the Cu surface and the graphene surface grooves according to the GBs of the annealed Cu surface, exhibiting a tight binding interfaces between the PDZ and the graphene/Cu foil. In Figure 3.6d, the Raman mapping data at the 2D band at 2685 cm^{-1} demonstrates that the graphene is uniformly coated over large areas (≈4900 μm^2) via lamination process.

From AFM analysis, again, we can check that as-synthesized GL-TE films have clean and smooth surface, without any polymer residues, wrinkles, tears, and any voids (Figure 3.7a), whereas the same structure fabricated by the conventional PMMA-assisted wet-transfer method had lots of surface perturbations in Figure 3.7b[11,44] (TG-TE).

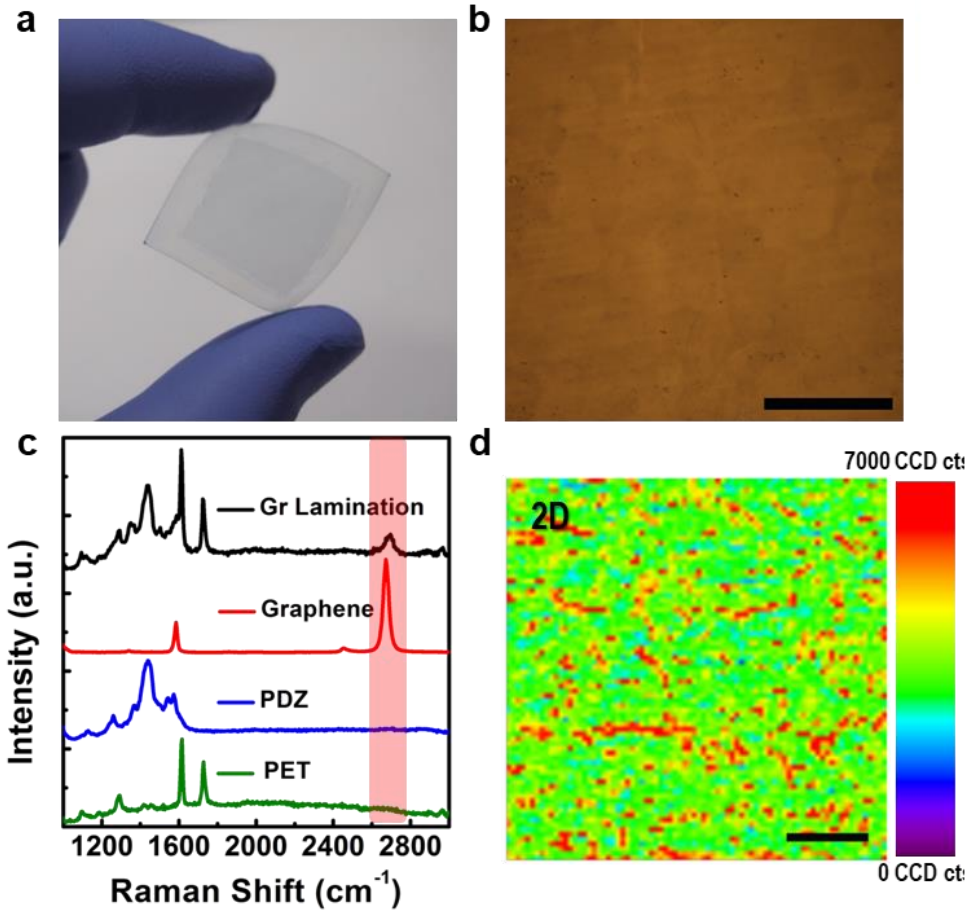

Figure 3.6. (a) The photograph image of large area of graphene-laminated PDZ film on PET substrate showing the transparency and flexibility. (b) Optical microscopy image (scale bar, 150 μm) (c) Raman spectra of PET(green), a PDZ film (blue), Graphene (red) and Gr lamination film (black) (d) Raman mapping of 2D band of Gr lamination film on PET (70 μm x 70 μm size).

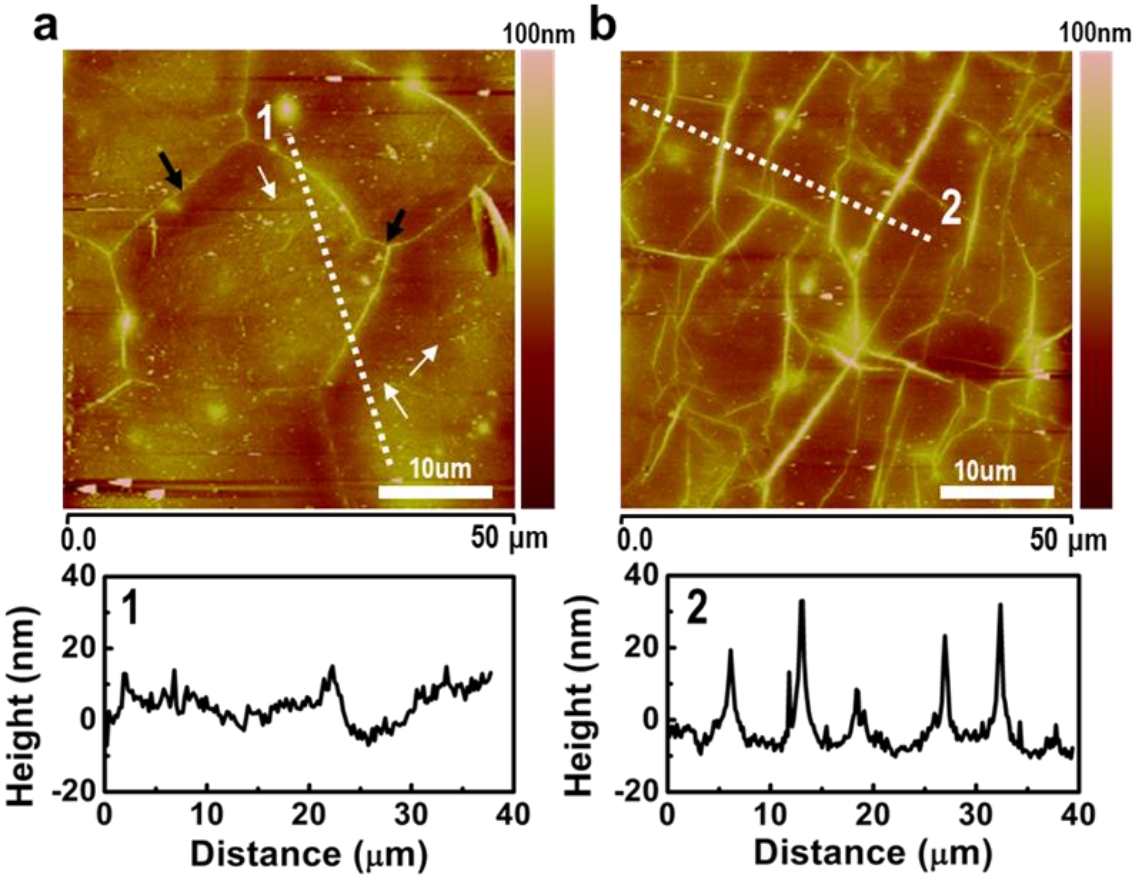

Figure 3.7. AFM data of graphene/PDZ structures fabricated by (a) lamination process and (b) conventional PMMA wet transfer process.

3.3.2 Electrical and optical characteristics of graphene-laminated transparent electrodes

In order to assess the electrical properties of the samples in terms of interface properties, the bare PDZ/PET sample and two graphene-based TE films fabricated by different processes (GL-TE and TG-TE) were measured using a CTLM method.[42,43] As shown in Figure 3.8b, the spacing distance affects the resistances. Though analysis the trends of different resistances with different spacing distance, we can deduce the fitted line in the measured data and make use of the information into the equation for CTLM method. The estimated R_c and R_s of the sample were 0.05 kΩ and 0.29 kΩ sq^{-1}, respectively, which were much lower than those of the TG-TE film (R_c = 0.14 kΩ, R_s = 0.47 kΩ sq^{-1}). This enhancement could affect the GL-TE film morphologies, with the decrease in the number of wrinkles, tears and air gaps.

Hall measurements were also implemented for the various TE samples through the van der Pauw method, in Table 3.1 and through comparing the results of reference conductive polymer samples to literature, we can confirm its validity.[36,37] Through Hall measurements, we can check that the charge carriers for all samples are p-type materials with mainly hole dopants. Notably, in the case of the GL-TE film samples, the room-temperature carrier mobility were measured to be 85.1 $cm^2\ V^{-1}\ s^{-1}$, exceeding to the TG-TE film (20.1 $cm^2\ V^{-1}\ s^{-1}$). For reference, the bare PDZ/PET film exhibited the carrier mobility of 1.95 $cm^2\ V^{-1}\ s^{-1}$ at room temperature. The changes in hall mobility indicates that an effective bypass was formed by the top layer of graphene, inducing a considerable transverse Hall voltage. Since the estimated charge carrier density decreased by more than two orders, the mobility of the GL-TE can be improved simultaneously. Compared to any conductive polymer-based flexible film, this mobility was much higher, as shown in Figure 3.8c. Therefore, conductive polymer-based TEs can be utilized by the lamination process and in the flexible optoelectronic applications such as organic light emitting transistor (OLET), which demands high operation speed.

Moreover, through the control of the PDZ thickness, we can reduce the sheet resistance for GL-TE, even though this method accompany with a trade-off in optoelectrical properties (Figure 3.8d). In order to evaluate the trade-off trends in GL-TE samples, we control the PDZ thickness by controlling the number of spin-coating process and laminate the PDZ/PET structure with Gr/PDZ added with D-sorbitol/multilayer. We can check that the sheet resistance of GL-TE samples initially decreased significantly as a result of the bulk resistance. At the third PDZ coating cycles, our GL-TE films exhibited an average sheet resistance of 48 Ω sq^{-1} with a transmittance of 79% (at 550 nm), comparable to other conductive polymer-based TEs with high optoelectronic properties.[36,37,38] In other words, further improvements in the optoelectrical properties of GL-TE samples can be obtained by controlling the composition of additives in PDZ solution and spin-coating parameters of the optimized solution.

In order to analyze the observed electronic properties, we tried to investigate the interfacial properties

of contact between the graphene film and PDZ layer in our samples via UPS. Through conventional estimation of work function, each GL-TE films, PDZ/PET and CVD-Gr/PET exhibited 5.12, 5.06 and 4.55 eV of work function, respectively (Figure 3.9a). It seems that carrier doping effects and charge transfer at the interface was accompanied by the disparity between the electron affinity of the PDZ film and the ionization potential of graphene. In Figure 3.9b, the electron charge transfer from the graphene to PDZ film can be induced by the potential disparity at the interface. In addition, the acidic sulfonic groups in the PSS region also can drag electrons from the graphene. As a result, the Fermi level of the graphene in GL-TE samples will significantly decreased from the Dirac point. Moreover, in Raman spectra, the p-type doping effect also can be observed through the change in the G peak position of graphene in Figure3.9c.[11,45] The position of G peak in the GL-TE film at 1616 cm^{-1} was blue-shifted by ~18 cm^{-1} from the position of G peak in CVD graphene at 1586 cm^{-1}, demonstrating the interfacial p-type doping of graphene in the GL-TE film.

The interfacial interactions of the GL-TE films were further investigated by XPS analysis in order to confirm the surface composition and chemical structure of the GL-TE films.[46] As shown in figure 3.9d, the S 2p core level spectrum of the Gr-laminated film was confirmed, exhibiting two primary peaks resulting from different chemical bonds. The S 2p peak around 162–166 eV, was derived from the overlap of the $2p^{1/2}$ and $2p^{3/2}$ states of the S atoms in the PEDOT parts. On the other hand, the other S 2p peak doublet around 166–171 eV, was derived from the S atoms in the PSS parts.[47,48] The intensity of S 2p peaks can estimate the molar ratio of PSS to PEDOT and the molar ratio of PSS:PEDOT in the GL-TE film can be estimated to be a much higher value of 6.5 than those of as-received PEDOT:PSS (2.5, Clevios PH 1000) or the PDZ film (2.9). In the preceding mention, the addition of Zonyl in the PEDOT:PSS films resulted in the phase segregation because of conformational changes of PEDOT, extending conducting PEDOT grains covered by the insulating PSS. In other words, an excess of PSS regions can be detected at the outermost film surface, as verified by depth-profiling XPS analysis (Figure 3.9e). Therefore, we suggest that lots of sulfonate groups in PSS strongly interact with the graphene at the surface of the GL-TE film, leading to p-type doping effect.

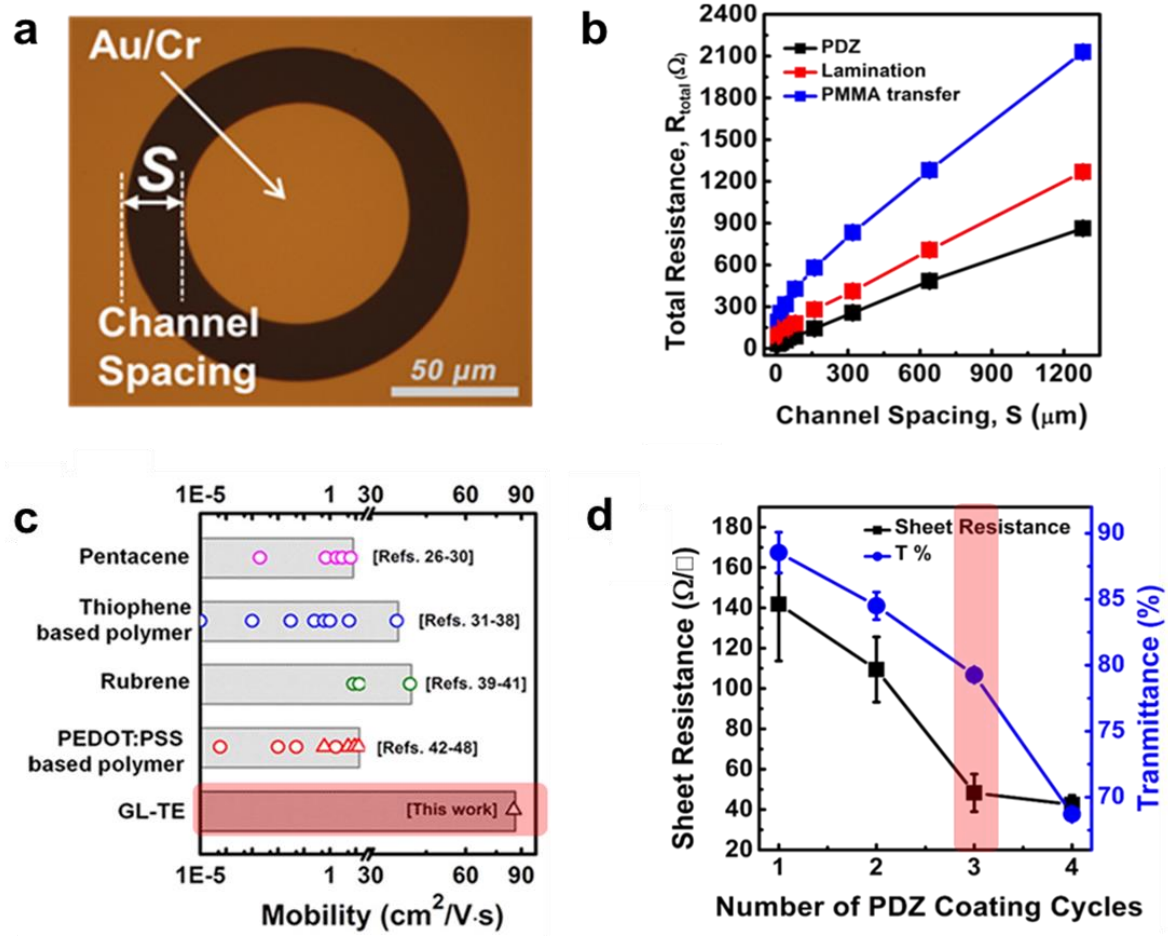

Figure 3.8. Electrical characteristics of GL-TE samples. (a) Optical microscope image of CTLM-patterned GL-TE sample. (b) Contact resistance between graphene and PDZ layers depending on the TE structure. Red line indicates our GL-TE sample and blue line indicates Gr/PDZ structure form by conventional wet transfer process. (c) Change in sheet resistance depending on the number of PDZ coating cycles.[72] (d) Hall mobility results of our GL-TE structure.

Table 3.1. Electrical characteristics of various flexible TE structures on PET under the same condition.

	Sheet Resistance (Ω/□)	Hall Coefficient R_H (cm^3/C)	Carrier Density N (cm^{-3})	Mobility μ ($cm^2/V{\cdot}s$)
PEDOT:PSS	**$205 \times 10^{+4}$** ± $420 \times 10^{+2}$	**0.390** ± 0.09	**$1.68 \times 10^{+19}$** ± $4.38 \times 10^{+18}$	**0.21** ± 0.08
PDZ	**119** ± 10.6	**0.002** ± 0.002	**$3.85 \times 10^{+21}$** ± $1.68 \times 10^{+21}$	**1.95** ± 1.59
TG-TE	**110** ± 27.2	**0.023** ± 0.012	**$3.17 \times 10^{+20}$** ± $1.13 \times 10^{+20}$	**20.1** ± 5.42
GL-TE	**120** ± 14.9	**0.155** ± 0.019	**$4.08 \times 10^{+19}$** ± $4.56 \times 10^{+18}$	**85.1** ± 6.35
CVD-Gr	**1390** ± 221	**0.072** ± 0.008	**$8.82 \times 10^{+19}$** ± $1.06 \times 10^{+19}$	**520** ± 61.9

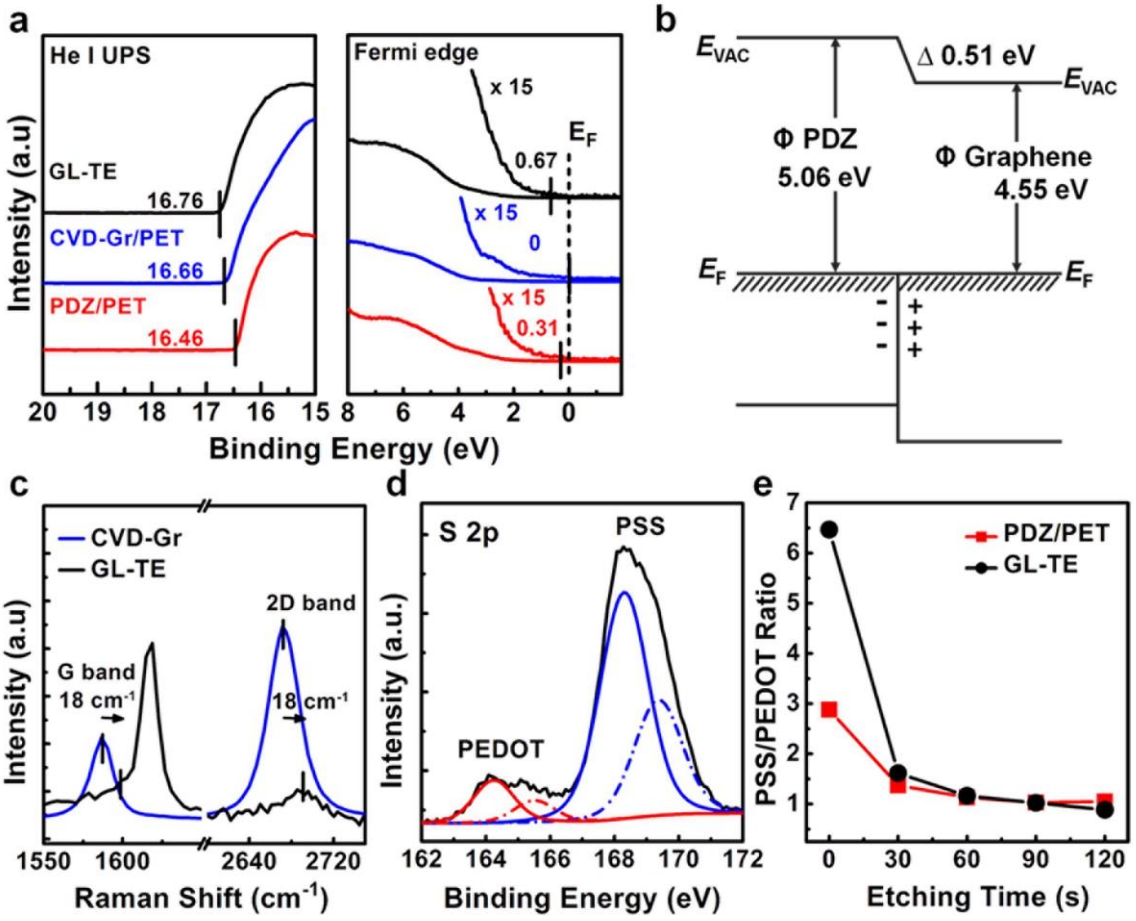

Figure 3.9. Optical characteristics of the surface and interface of GL-TE structure. (a) Ultraviolet photoelectron spectroscopy of three different types of films. (b) Energy level diagram of GL-TE samples. (c) Raman spectra of CVD-Gr on SiO_2/Si substrate (blue) and GL-TE film (black), showing a blue shift of 18 cm^{-1} for G and 2D peaks of graphene. (d) High resolution XPS spectra of S 2p of the GL-TE film. (e) Depth profiling of the ratio of PSS to PEDOT.

3.3.3 The role of graphene in the charge transport of the hybrid structure

In order to analyze the role of graphene in GL-TE structure in terms of the lateral charge transport, the temperature-dependent electrical conductivities of three different samples, such as GL-TE films, CVD-Gr/PET, and bare PDZ/PET were measured. In figure 3.10a, conventional semiconductor behavior of PDZ/PET was confirmed, showing the increase in resistivity with a decrease in temperature. The laminated sample also exhibited a semiconducting behavior with a lowered variation than one of the bare PDZ/PET film. The temperature-dependent conductivity behavior of disordered materials (e.g., hopping transfer) can be analyzed by the variable range hopping (VRH) model as follows,

$$\sigma(T) = \sigma_0 \exp\left[-\frac{T_0}{T}\right]^x \quad (1)$$

where T_0 is a characteristic temperature that can be considered as an effective energy separation between neighboring localized states[49] and the exponent x corresponds to 1/(1 + D) where D indicates hopping dimensionality in conducting system. In order to obtain x & D value, equation (1) must be converted in terms of the reduced activation energy, $W = -d(\log \rho)/d(\log T)$, as follows,

$$\log W \approx \log(xT_0^x) - x \log T \quad (2)$$

From the linear slope of the log W versus log T plot, we can determine the x value and also the hopping dimension D in the disordered system. The y intercept indicates the characteristic temperature T_0. As shown in Figure 3b, we can confirm the temperature dependence on the reduced activation energy for the PDZ/ PET and the GL-TE films. For the PDZ/PET film, the estimated linear slope x was 0.358, which corresponds to the 2D-like VRH transport according to x = 1/(1 +D). From the equation, the measured characteristic temperature T_0 was 531 K. Again, since the addition of DMSO in pristine PEDOT:PSS promotes the elongation of the PEDOT chains, the PEOT region with closer links between each other resulted in elliptical PEDOT grains.[49–51] Moreover, addition of Zonyl in PEDOT:PSS further formed lamellar segregation between PEDOT regions and PSS regions.[36] This morphological change in PEDOT:PSS may lead to quasi-2D transport, leading to strong anisotropy between in-plane and out-of-plane conductivities.[52] The inset of Figure 3.10a shows excellent linearity in the plot of σ(T) versus $T^{-1/3}$ for PDZ/PET film. For GL-TE films, the slope of log W versus log T plots has been hugely lowered, as shown in Figure 3.10b. Moreover, the plot of log W versus log T shows an apparent deflection point at around 40 K. The graphene top layer in GL-TE films starts to be a dominant current path below 40 K, showing nearly temperature independent trends of CVD graphene compared to that of PDZ film. On the other hand, above 40 K, the PDZ layer starts to serve as a dominant transport route. In the plot of reduced activation energy, the significantly lowered x value reflects that the graphene layer still serves

as an effective transport bypass even at high temperature. Through our temperature-dependent investigation (Table 3.2), the changes in dominant charge transport behavior are clearly demonstrated. In other words, the dominant charge transport of our GL-TE film mainly occurs in the PDZ film at room temperature and the laminated graphene top layer also serves as a effective bypass for charge carriers in this hybrid system.

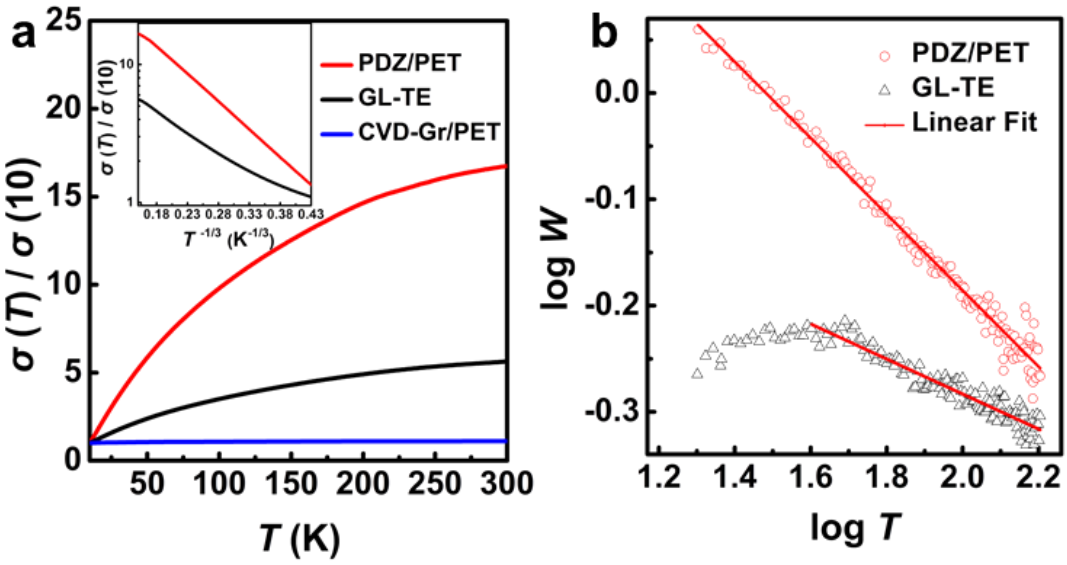

Figure 3.10. Characterization of temperature-dependent charge transport behaviors. (a) Changes in the conductivity as a function of temperature. (b) Changes in the activation energy as a function of temperature. Red lines are the linear fitting line in order to estimate VRH transport dimensionality.

Table 3.2. Temperature-dependent electrical characteristics of the four types of organic electrodes.

	σ (10 K)	σ (300 K)	R_s (10 K) [$\Omega\,\square^{-1}$]	R_s (300 K) [$\Omega\,\square^{-1}$]	σ (300)/σ (10)
PD/PET	31 [S cm^{-1}]	543 [S cm^{-1}]	3223	184	17.5
PDZ/PET	34 [S cm^{-1}]	584 [S cm^{-1}]	2869	171	17.1
GL-TE	118 [S cm^{-1}]	667 [S cm^{-1}]	845	150	5.6
CVD-Gr/PET	1.00×10^{-3} [S]	1.11×10^{-3} [S]	996	898	1.1

3.3.4 Environmental stability tests of graphene-laminated transparent electrodes

Operational stability under various unfavorable mechanical strains and outdoor conditions is a very critical issue for practical applications. The effect of mechanical bending on our GL-TE films were evaluated using 5000 consecutive bending cycles as shown in figure 3.11a, showing the change in the resistance of the GL-TE films as a function of the number of bending cycles. During the 5000 bending cycles of around 7.6% strain, the GL-TE films showed that their on-and-off performance was maintained and exhibited a promising mechanical bending stability. In addition to bending stress, the active component materials must also have high stretchability for the use in practical flexible TE devices.[53] In order to evaluate the stretchability test, we prepared bare PDZ and GL-PDZ films on poly-urethane acrylate (PUA) substrates and measure the change in the resistance as a function of tensile strain. In terms of plastic substrates, PUA substrate showed better stretchable property than PDMS (Figure 3.12). Figure 3.11b shows the change in the resistance as a function of tensile strain. Until the 23% of tensile strain, in the case of the bare PDZ/PUA film, the resistance increased steeply, by over 1.6 kΩ, whereas the resistance of the GL-PDZ/PUA film relatively maintained from its original resistance, showing the increased by only 0.57 kΩ. As previously mentioned, the conformal graphene top coating layer provided effective conducting paths for charge transport by covering the damaged PDZ parts during the stretchability test. Above ~23% of tensile strain, however, the resistance of the GL-PDZ/PUA film also steeply increased, indicating an occurrence of fracture inside the GL-TE sample.

In order to evaluate the operational stability, UV light, high humidity and thermal stress were applied to bare PDZ/PET and GL-TE films, the changes in their resistance were measured as a function of time under UV light irradiation and humidity. In figure 3.11, our results demonstrated that graphene barrier can protect the GL-TE samples from the exposure of the samples to UV light (λ = 254 nm). During 3 h of UV light exposure, in the case of the graphene-free bare PDZ/PET samples, the resistance rapidly increased above 3 kΩ, whereas the resistance of the graphene-laminated our samples increased to only 0.72 kΩ, showing an 4.5 times slower increase in resistance. On the other hand, in order to evaluate the stability under high humidity, water permeation experiments at 80% humidity was set up. The graphene laminated samples did not show huge degradation in resistance significantly for 30 h (Figure 3.11d). In contrast, the resistance of the bare PDZ/PET films without graphene top layer, showed a relatively huge change but linear slope until 15 h of exposure; after 15 h, a sudden large oscillation occurs with steep increase in resistance. Therefore, introduction of a conformal graphene coating provided a barrier property on organic layer under UV light and moisture significantly, while the resistance showed little change and increased only to 0.28 kΩ.

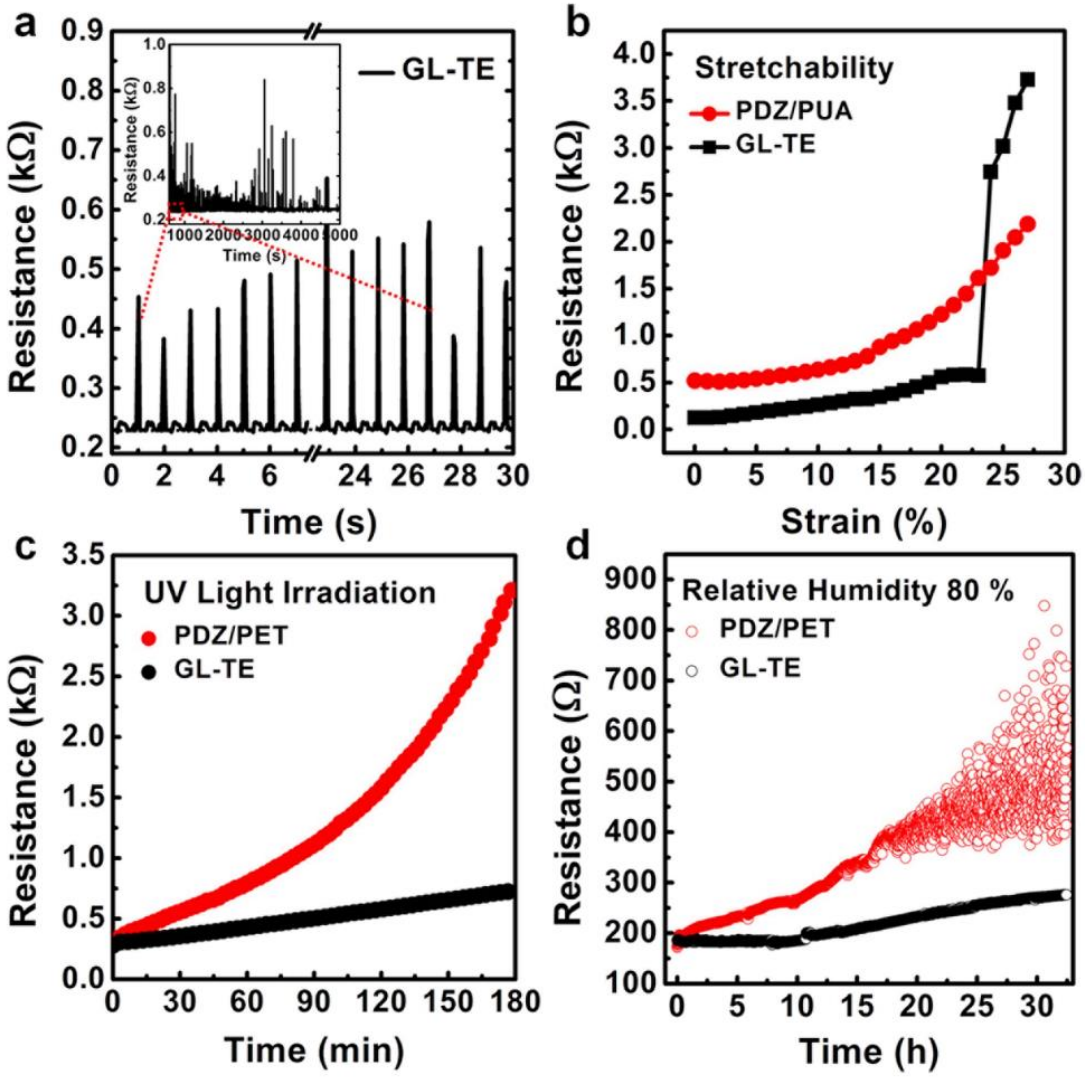

Figure 3.11. Evaluation of environmental stability of GL-TEs. (a) Bending stability tests at 7.6% strain. (b) Stretchability test of the PDZ (red) and GL-TE (black) films on polyurethane substrates depending on tensile strain. Operational stability tests under (c) exposure to UV light (λ = 254 nm) with an power of 6 W and (d) moisture >80 RH%.

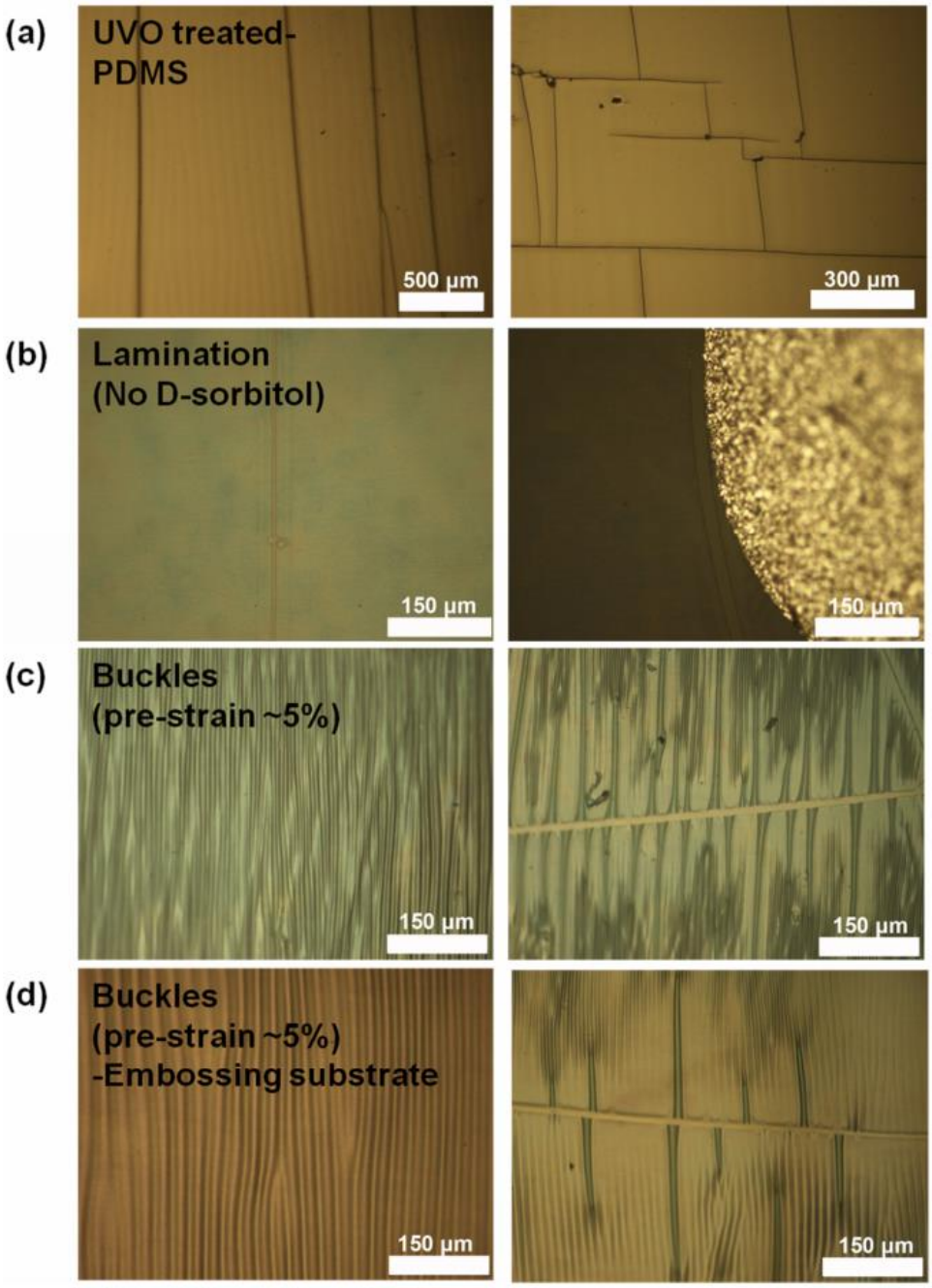

Figure 3.12. Inherent limitations of PDMS substrate in stretching or strain test. (a) The facture surface of UVO-treated PDMS with longitudinal and transverse cracks measured without prestrain procedure. (b) The silver electrode on a GL-TE film placed on a PDMS substrate can produce cracking around the metal electrode owing to the surface energy difference between the electrode and the PDMS substrate. (c-d) Formation of transverse cracks in GL-TE films (c) on a pre-strained (~5%), planar PDMS substrate and (d) on a pre-strained (~5%) embossing type-PDMS substrate after releasing pre-strain. Note that the compressive strain along the perpendicular direction of the uniaxial tension of the pre-strain can induce transversal crack lines.

Previous operation stability evaluation for the barrier properties of GL-TE films drives their possibility in the use of thermal-resistant coatings. For another operational stability in terms of thermal stress, a four-point probe station equipped with a heating stage was set up with temperatures ranging from 25 to 200 °C. In Figure 3.13a, in the case of bare PDZ/PET film, the sheet resistance increased by ~21% till 150 °C, whereas the sheet resistance of the GL-TE film increased by only ~8%. The conformal graphene top layer coating offers a significant improvement in the thermal conductivity and thermal stability of the organic compounds. Since the PET substrate with low glass transition temperature is thermally degraded above 150 °C,[54] there was the abrupt increase in the sheet resistance of the GL-TE film. As another thermal stability test, TGA of the PEDOT:PSS, PDZ, and GL-TE films was implemented in order to analyze the role of graphene for the thermal spreading layer on the stability of the conductive organic compounds and evaluated their lifetimes by decomposition kinetics.[52–54] Through TGA analysis, the weight loss was monitored as a function of increasing temperature with a heating rate of 10 °C min^{-1} (Figure 3.3). In the early stage of temperature range around 100–200 °C, the weight loss occurs gradually on the both the Gr-free PEDOT:PSS and PDZ films, due to the water evaporation. Next, above 300 °C, a significant weight loss of both two samples was observed, as expected, suggesting that the fragmentation of the sulfonate group occurred.[58] Compared to bare PDZ/PET films, the GL-TE films exhibited considerably enhanced thermal stability up to 700 °C (Figure 3.13b). In other words, introduction of graphene monolayer onto organic TE films contribute to the higher overall stability in the GL-TE film due to the outstanding thermal dispersion of the graphene layer.[6,59]

From the TGA results of the PEDOT:PSS, PDZ, and GL-TE films and Toop's relation, we can further analyze stability for thermal degradation and the estimated lifetime by decomposition kinetics (also see Figures 3.3–3.5).[60–62] Figure 3.13c demonstrated that the estimated lifetime of GL-TE films remarkably was much higher than the one of other samples; for example, it is expected that the GL-TE samples are stable for more than 105 h at ~150 °C. The estimated lifetime of GL-TE is longer than that of Gr-free PDZ films by two orders of magnitude, demonstrating that the monolayer graphene coating contributes to a high-quality heat barrier on organic TE films.

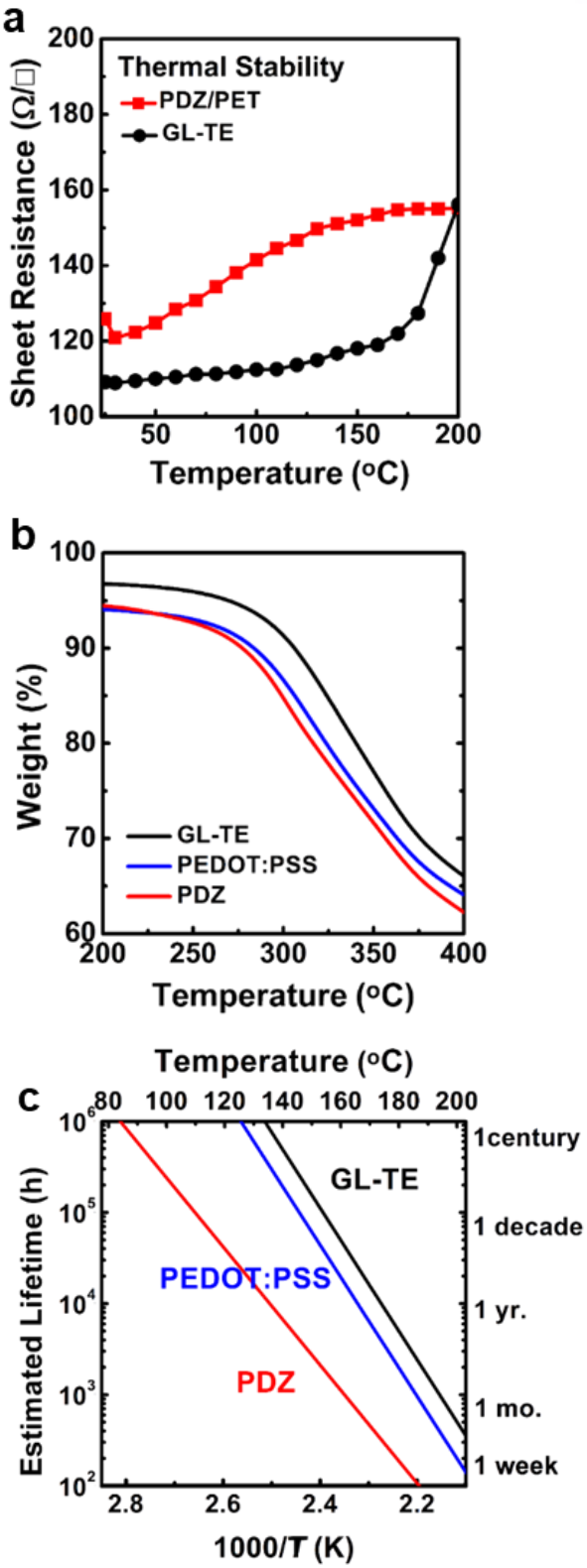

Figure 3.13. Evaluation of thermal stability and estimated lifetime of the graphene-covered organic films. (a) Changes in the sheet resistance of as a function of temperature. (b) TGA analysis of different types of organic films at a constant heating rate of 10 °C min^{-1} in N_2 atmosphere. (c) Estimated lifetimes deduced by Toop's relation for different types of organic films.

3.4 Summary and Outlook

Through facile functionalization of PEDOT:PSS, Gr/functionalized PEDOT:PSS composites can potentially serve as an alternative TE for commercial optoelectronic applications. The construction of a TE composite with clean interfaces is prerequisite for preserving their pristine properties. However, in the use of CVD graphene, transfer process is unavoidable and needless organic supporting layer lefts residual contaminants and some damages on graphene surface, leading to poor interface property between graphene and PEDOT:PSS layers. Additional functionalization of PEDOT:PSS with D-sorbitol gives adhesive property to PEDOT:PSS layers and enables direct transfer of graphene onto target plastic substrate using the functionalized PEDOT:PSS supporting layers, while keeping clean surface of as-grown CVD graphene.

In this chapter, we devised a novel direct transfer method using lamination process for fabrication of Gr-based organic TE films. Direct transfer method provided a effective way for formation of Gr-laminated structures without interfacial perturbations such as organic residue, tears or defects from the transfer process, leading to great optoelectrical properties. Moreover, the operational stability for organic films can be enhanced by using 2D carbon materials. In the case of GL-TE films, the PDZ layer laminated by monolayer graphene can endure various unfavorable conditions, compared to bare PDZ layer. The estimated lifetime of GL-TE samples for thermal degradation was expected to be longer than bare PDZ samples, by two orders of magnitude. It is also be noted that the graphene-lamination process is not finite to the PEDOT:PSS films and we expect similar strategy to be designed for other materials and their applications. Our results can pave the way for realization of graphene-based organic TE materials with excellent optoelectrical performance and great long-term stability, which is superior to ITO, for flexible organic optoelectronic applications.

Chapter 4. Fabrication of Graphene/Acid-Treated PEDOT:PSS Anode through Colorless Polyimide-Assisted Direct Transfer Process for Flexible Polymer Light Emitting Diode(PLED)

4.1 Introduction

Transparent electrode(TE)s for flexible organic light-emitting-diodes(OLED)s require for excellent electrical conductivity, high optical transmittance. ITO is a representative TE materials owing to excellent optoelectrical performance and electrochemical stability. However, although it has excellent properties, its high cost, poor mechanical properties and the high-temperature fabrication methods limit the use of ITO in flexible applications.

Selection of appropriate flexible substrates is another important factor for flexible TEs. Among them, polyimide has been widely used in flexible optoelectronics, due to its higher heat resistance over 350 °C and low coefficient of thermal expansion (CTE) below 10 ppm.[60–62] However, due to its insolubility, solution processing of polyimide is almost impossible, and its opaqueness and yellowness of PI (transmittances of <70% at 550 nm[66,67]) limit the use of substrates in optoelectrical applications. The intramolecular and intermolecular charge transfer complex (CTC) effect results in the opaqueness and yellowness of PI. In order to reduce CTC effect, an addition of the trifluoromethyl group which has high electronegativity, or a bent structure was designed for transparent colorless polyimide (TCPI) with the weak intermolecular interaction. However, not only the trade-off between the thermal and optical properties, but also the yellowness of the TCPI still remain a difficulty to be solved for its practical use in optoelectronic applications. Therefore, lots of efforts on designing the solvent-soluble TCPI by changing dianhydride and diamine monomer components without sacrificing its excellent properties have been developed.

In this chapter, we devised solution-soluble TCPI-assisted fabrication of Gr-based organic TE for realization of flexible PLED application. The trilayer composite consisted of monolayer graphene (Gr) film-intercalated a methanesulfonic acid (MSA)-treated PDZ (MSA-PDZ) and a transparent and colorless polyimide (TCPI) layer. The direct formation of high-quality graphene through a solution-processable TCPI, resulting in a clean interface. MSA-PDZ layer provide a stable doping effect on graphene, enabling the graphene-based TE film to have adequate optoelectrical properties and work function. Moreover, TCPI/Gr/MSA-PDZ structure showed a high figure of merit of ~70. For operational and long-term stability tests, Gr-intercalated TCPI/PDZ structure had excellent endurance under unfavorable environmental conditions, such as exposure to moisture and mechanical and thermal

stresses. Furthermore, owing to the synergy effect from trilayer geometry, the TCPI/Gr/MSA-PDZ anode-based PLED exhibited excellent current and power efficiencies, superior to those of ITO based PLEDs. Moreover, TCPI/Gr/MSA-PDZ anode-based PLED can endure over 500 cycles of bending test at the bending radius of 5 mm. The graphene-based trilayer composite showed great potential for practical use in large-area flexible optoelectronics and, owing to excellent optoelectrical performance and operational stability, is a promising candidate for next-generation flexible optoelectronic devices.

4.2 Experimental section

Fabrication of CVD graphene on electropolished Cu foil.

CVD graphene monolayer was grown on a 25 μm-thick Cu foil through the LPCVD system. First, a Cu foil was cleaned using sequential sonication in acetone and isopropyl alcohol solutions (IPA), followed by blow-drying with N_2 gas. For surface treatment of Cu foil, electropolishing in phosphoric acid for 10 min was proceeded, providing a removal of contaminations (e.g., amorphous carbon, metal impurities) on the Cu foil smooth surface. Followed by electropolishing process, the Cu foil was rinsed with DI water and IPA rinsing. The air-oxidized Cu foil was dragged into a furnace and the sample was annealed till T of ~1050 °C by flowing H_2 gas of 100 sccm. As soon as T approach 1050 °C, the condition was kept for 35 min. Then, to diminish the native oxides on graphene surface, including amorphous carbon, the sample was annealed for 1h. Then a CH_4(5 sccm)/H_2(100 sccm) gas mixture was introduced into the LPCVD system for 10 min (graphene growth step). After the graphene growth, the quartz tube was slowly cooled to ~600 °C at constant introduced flow and then fastly cooled down to RT under a hydrogen gas flow (30 sccm).

Polymerization and Characterization of Solvent-Soluble TCPI.

TCPI films which is solvent-soluble, were polymerized through melt-polymerization process of a mixed dianhydride and diamine monomers with a molar ratio of 2:1:1. (Dianhydride monomer: 4,4-(hexafluroisopropylidene)diphthalic anhydride (6-FDA), Diamine monomers: 4,4′-diaminophenyl sulfone (DDS), and 4,4′- (1,4-phenylenediisopropylidene)bisaniline (Bis-P)) The mixture of each monomer in an alumina boat was annealed at 300 °C under a N_2 atmosphere for 1 h. After melt-polymerization was finished, we can check fine yellow powders were synthesized well. For structural characteristics analysis, proton nuclear magnetic resonance (1H NMR) measurements were implemented using a 400 MHz Bruker 400 NMR spectrometer with DMSO-d_6 and tetramethylsilane (TMS) as an a solvent and internal standard, respectively. In order to evaluate structural characteristics of TCPI, Fourier transform infrared spectroscopy (FT-IR) and gel permeation chromatography (GPC) studies were implemented using a Varian 670/620 spectrometer and an Agilent 1200S instrument, respectively. The TGA and differential scanning calorimetry (DSC) measurements were performed for thermal characteristics of TCPI using TA Instruments Q500 and Q200, respectively. (During TGA and DSC analysis, heating rate was kept at 10 °C/min. Glass-transition temperature ($\underline{T}_g$) for our TCPI materials was checked by the conventional midpoint method.)[68,69]

Design, fabrication and characterization of TCPI/Gr/MSA-PDZ composite TEs.

As-grown Gr/Cu foil is spin-coated by the solvent-soluble TCPI solution at 1000 rpm for 60 s and

annealed in a vacuum oven at 200 °C for 12 h. Next, the Cu foils were removed by an aqueous solution of 1 M APS. For functionalization of PEDOT:PSS, PEDOT:PSS solutions were added with DMSO and Zonyl fluorosurfactant. In the subsequent procedure, the Gr/TCPI was covered with PDZ layer through the spin coating of 3000 rpm and annealed at 120 °C for 20 min, in ambient conditions. Methanesulfonic acid (MSA) with $pK_a \sim -1.9$, was utilized for an additional functionalization of the PDZ films, followed by heating at 160 °C for 3 min.

The structural characteristics of the TCPI/Gr/MSA-PDZ, TCPI/Gr and CVD graphene samples were analyzed via tapping mode AFM. In order to obtain Raman spectra, functionalized PDZ films were prepared on SiO2/Si and CVD-Gr on SiO2/Si samples. The model of Raman equipment is WiTec alpha 300R. The micro Raman system has a excitation source of 532 nm with the laser size of ~640 nm for a ×50 objective lens with 0.9 numerical aperture, we can implement the Raman spectroscopy and mapping. The Raman data was confirmed by checking more than 10 different spots per sample. A spectroscopic image of Raman mapping was obtained by measuring the Raman spectra of each individual pixel around the 2D peak of graphene, with a 60 μm × 60 μm area using WiTec Project software. More than 10 different positions per sample were detected as Raman spectra for accuracy. UV−vis−NIR spectroscopy (Varian, Cary 5000 model) was implemented to measure the optical transmittances (T_r) of samples within a wavelength range of 300−800 nm. We measure the transmittance at a wavelength of 550 nm. Conventional four-point probe method was evaluated in order to measure the sheet resistances (R_s) of the thin films with a Hall effect system (Lakeshore Model 642). For mechanical stability test of 2 × 2 cm^2 samples, the bending tests were implemented by using a customized multi-specimen test system (UMT-2 T, Bruker Nano Inc.) with customized a 2-point probe potentiostat (Ezstat, CETR) and other components. In order to evaluate gas barrier effect of graphene, water vapor transmission rate (WVTR) analysis was introduced by using a PERMATRAN-W 3/33 MG PLUS (MOCON) equipment at 38 °C and 100 RH% with a detection limitation of 0.005 g m^{-2} per day. The N_2 carrier gas conveys water vapors penetrating the test film and detected by the inner infrared sensor. UPS measurements were performed to investigate the work functions of the samples on an Axis-NOVA (Kratos. Inc.) (base pressure 10^{-7} Pa) with a pass energy 1.0 eV at 0.05 eV per step, using the non-monochromatic He I radiation (21.2 eV). An atomically clean Au help to measure the energy calibration and ensure accurate values for Fermi edge before measurement, while applying −15 V bias for enhancement in the secondary photoelectron cut-off. UPS measurements was implemented to measure the work function of samples, which can be measured from $\phi_\upsilon = h\upsilon - |E_{cutoff} - E_{FE}|$, where $h\upsilon$ = 21.2 eV (He I source), where E_{FE} is the Fermi edge and E_{cutoff} is the onset of secondary emission cut-off edge.

Fabrication and Characterization of Flexible PLEDs.

For fabrication PLEDs with anode bottom structure, Our TCPI/Gr/MSA-PDZ samples were spin-coated by, as a hole injection layer, PEDOT:PSS (AI4083, Clevios) with 5 wt % Zonyl solution at 5000 rpm for 40 s, followed by annealing on a hot plate at 130 °C for 10 min. Next, as an active layer Super Yellow (SY) (PDY-132, Merck) solution, which is dissolved in chlorobenzene solvent with a concentration of 6.5 mg mL^{-1} at 80 °C, was spin-coated onto previous bottom structure at 2000 rpm for 45 s. As an electron injection layer and cathode material, a LiF (1 nm)/Al (100 nm) cathode was deposited by thermal evaporation processes in high vacuum (~10^{-7} torr), with deposition rates of 0.1 and 1.0 Å s^{-1}, respectively. The J−V−L characteristics of the flexible PLEDs were analyzed using a Keithley 2400 source measurement unit and a Konica Minolta CS-2000 spectroradiometer, before and after cyclic bending. At least 10 devices were measured for the average value of the PLED performance for accuracy.

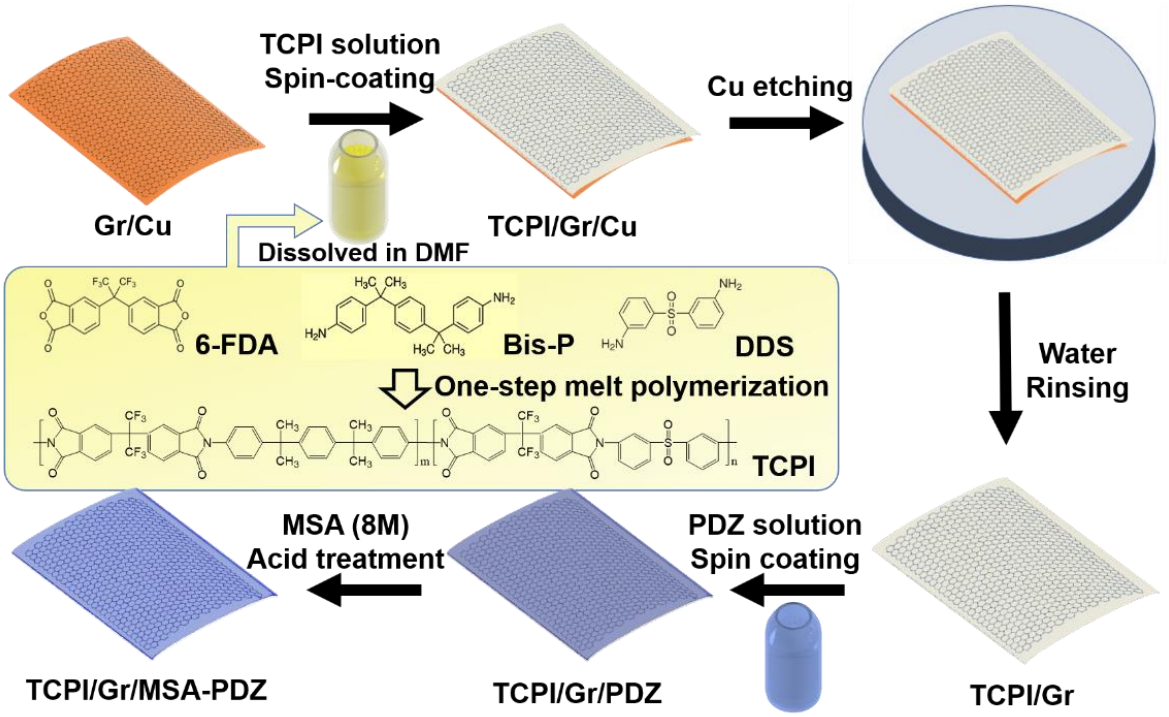

Figure 4.1. Schematic illustration for the fabrication of graphene-intercalated films using a solvent-soluble TCPI and simple melt-polymerization process.

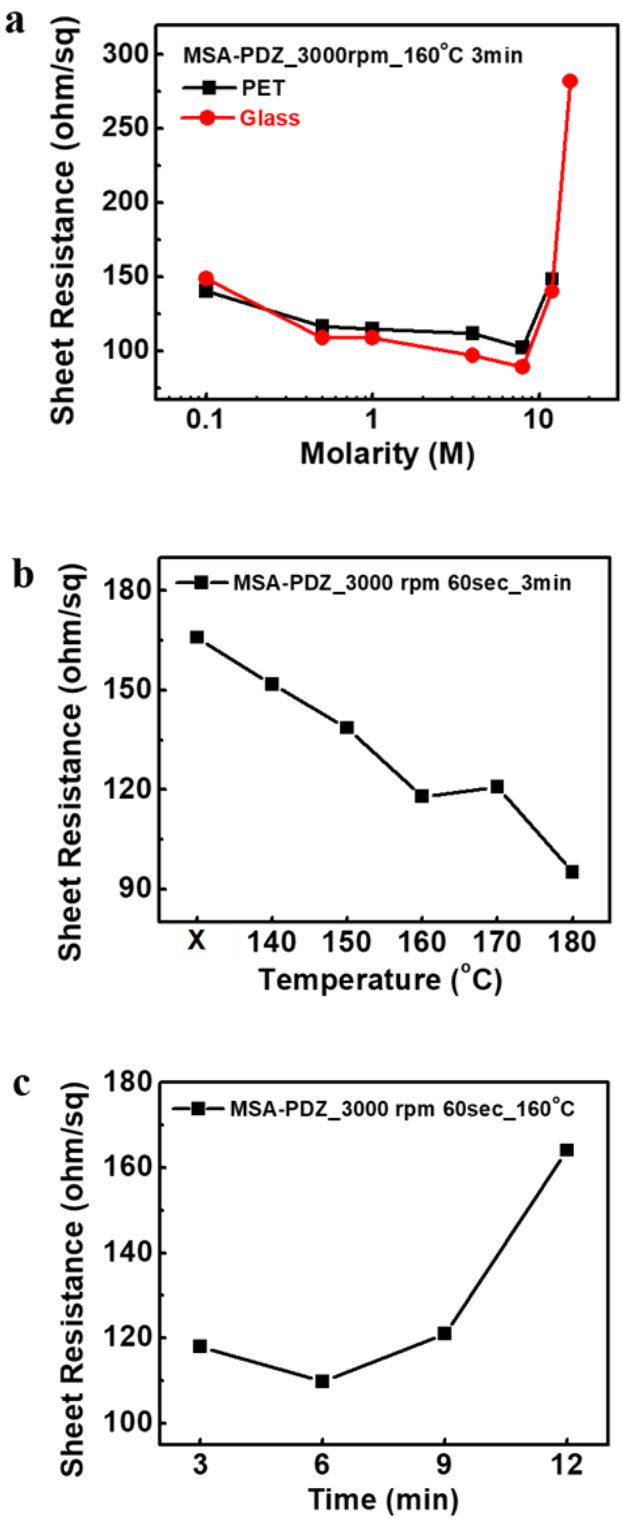

Figure 4.2. Acid treatment for an functionalization of PDZ film using methanesulfornic acid in terms of (a) the number of molarity of acid solution, (b) annealing temperature during acid treatment and (c) acid treatment time.

4.3 Results and discussion

4.3.1 Structural characteristics of TCPI/Gr/acid-treated PDZ

For successful fabrication of graphene-based composites, we introduce simple polymerization method for synthesis of TCPI. The soluble TCPI was synthesized via one-step meltpolymerization of one dianhydride (6-FDA) and two diamines (DDS and Bis-P) powders. The sulfone group ($-SO_2$) of DDS affects the optical transmittance of TCPI by decreasing the intermolecular CTC effect of the imide chains, and the methylene linkage from the Bis-P monomers enhances the mechanical and thermal stabilities of TCPI.[67] Through various analysis, such as NMR, FT-IR and GPC, the compositions of TCPI were confirmed by ^{1}H NMR and FT-IR spectroscopic studies. The aromatic ring hydrogen atoms of TCPI gave signals observed between ~8.25 ppm and ~7.15 ppm and the two representative peaks of PAAs at ~13.29 ppm (due to the carboxylic acid group) and ~10.32 ppm (due to the amide groups) were absent.[67,68] In addition, strong FT-IR peaks originating from long-chain imide groups were observed at ~1,785 cm^{-1} (C=O, in phase), ~1,724 cm^{-1} (C=O, out of phase), and ~1,367 cm^{-1} (C-N-C). The peak at ~3,500 cm^{-1} , corresponding to the amic acid groups, also absent due to chemical cyclization.[70,71] High molecular weight of the as-synthesized TCPI was confirmed by GPC measurement. These structural characteristics demonstrated that the simple one-step melt polymerization process enables successful synthesis of TCPI. Furthermore, from the DSC and TGA analysis, the results showed excellent thermal tolerance of a high T_g of ~245.3 °C and a high initial thermal decomposition temperature (T_{id}) of ~433.4 °C for the as-fabricated TCPI samples.

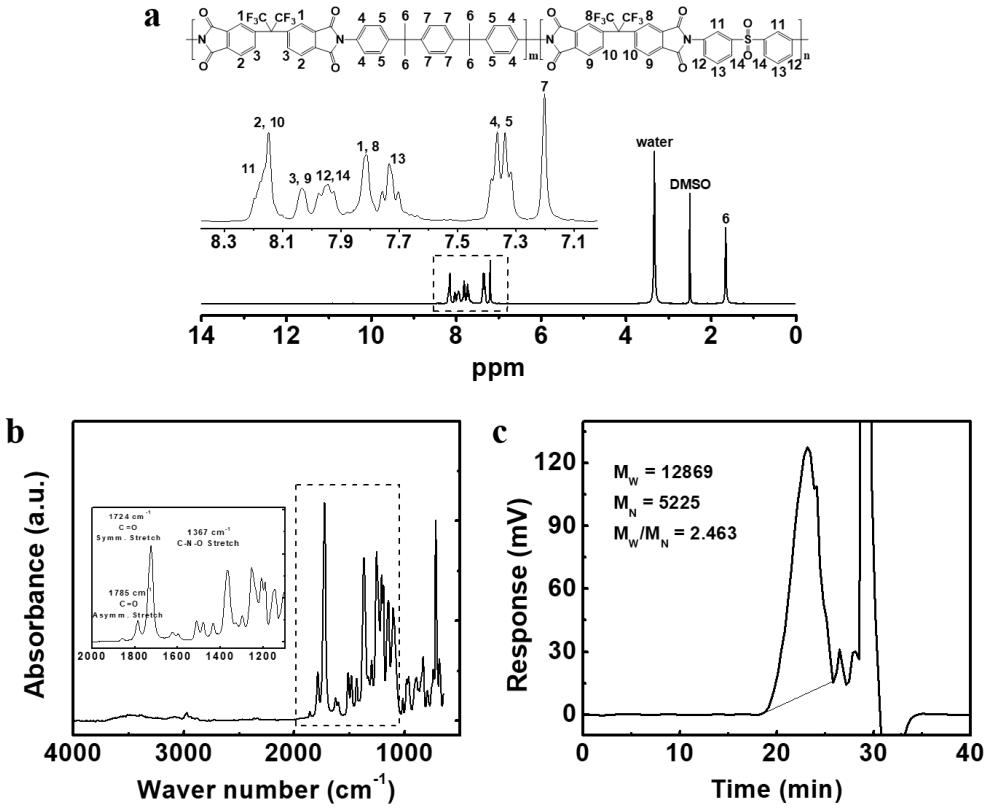

Figure 4.3. Analysis of structural characteristics of synthesized polyimide (TCPI). (a) ^{1}H NMR, (b) FT-IR and (c) GPC spectra of TCPI film derived from 6FDA, DDM, and DDS.

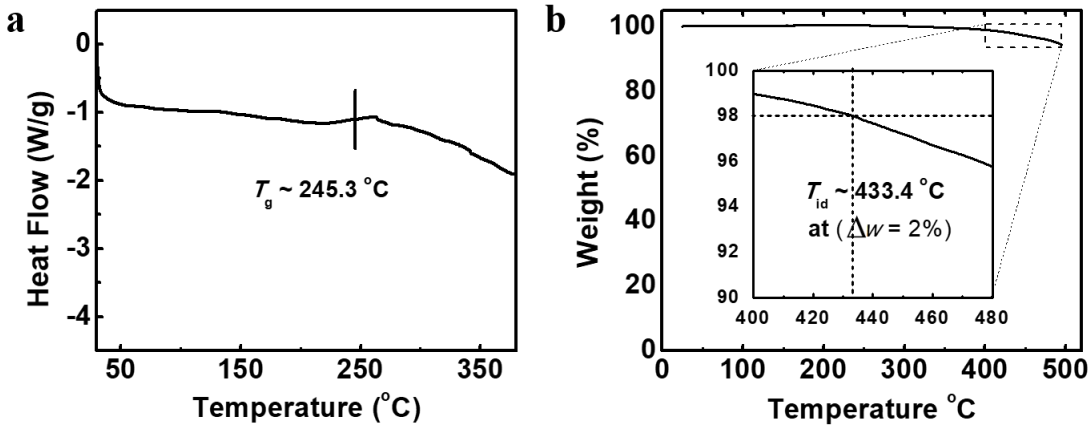

Figure 4.4. Thermal characteristics of transparent and colorless polyimide. (a) DSC and (b) TGA analysis of TCPI film.

4.3.2 Structural characteristics of TCPI/Gr/acid-treated PDZ

For fabrication of graphene-based organic TE structure, as-grown Gr/Cu foil was spin-coated by the TCPI solution at 1000 rpm for 60 s, then was annealed in a vacuum oven at 200 °C, over 12 h. Next, the growth template which is Cu foil was etched by using ~1.0 M of APS solution. Due to the hydrophobic nature of TCPI and the good wetting properties of DMF solvent, TCPI was successfully formed with monolayer graphene, conformally and uniformly. As shown in Chapter 2 and 3, the electrical conductivity of PEDOT:PSS,[72,73] was enhanced by an addition of a polar secondary dopant DMSO. Moreover, the wetting properties of the solution,41,45 can be improved by the fluorosurfactant, enabling the PDZ films to be coated successfully onto TCPI, PET or graphene which are super hydrophobic. For formation of graphene-based heterostructure, the PDZ film was spin-coated onto graphene/TCPI without any interfacial disturbance, leading to stable doping of graphene. Moreover, further enhancement of optoelectrical performance, new additional functionalization of PDZ was treated using methanesulfonic acid (MSA) with pKa approximately −1.9, followed by heating at 160 °C for 3 min. The insulating region of PSS^- was washed by acid treatment of MSA, through oxidization of PSS^-, enhancing the electrical conductivity significantly.[43] Figure a and b indicates the photographs and the corresponding Raman spectra of the as-fabricated TCPI/Gr/MSA-PDZ TEs, respectively. The Raman spectra indicate the successful integration of the Gr-intercalated flexible TEs.[22,23,72]

High-quality and large-area CVD-Gr on the organic surfaces can be formed using a simple TCPI solution process. Conventional polyimide with its insolubility and infusibility property was hard to be obtained by solution process, there usual polyimide can be obtained by coating and annealing poly(amic acid) (PAA) which is an intermediate precursor.[74] However, the PAA-assisted procedure is hard to adapt in graphene-based composite due to differences of hydrophobicity between the hydrophilic nature of PAA and graphene, In addition, by-products from imidization, such as water, can lead to poor adhesion between graphene and polyimide, resulting in peel off of the PI film, as shown in Figure 4.5d. On the other hand, solvent-soluble TCPI can be used for direct fabrication of as-grown CVD graphene with the large sample size, over 7 × 7 cm^2 (Figure 4.5a), owing to the hydrophobic nature of TCPI. Through Raman mapping of the graphene 2D peak, we can confirm the presence of large-area graphene over TCPI substrates. (Figure 4.5e). In Figure 4.5c, the graphene directly formed onto TCPI show clean with a smooth surface, without any wrinkles, air gaps, tears, or PMMA residues, using optical microscopy (OM) and atomic force microscopy (AFM) analysis method, in contrast with the surface of CVD graphene transferred by conventional PMMA wet transfer method (Figure 4.5d).[23,68,75,76] Moreover, the MSA-PDZ coated Gr/TCPI film exhibit enhancement of the optoelectrical properties as well as reduction in the surface roughness of TCPI/Gr down to ~1.5 nm (Figure 4.6).

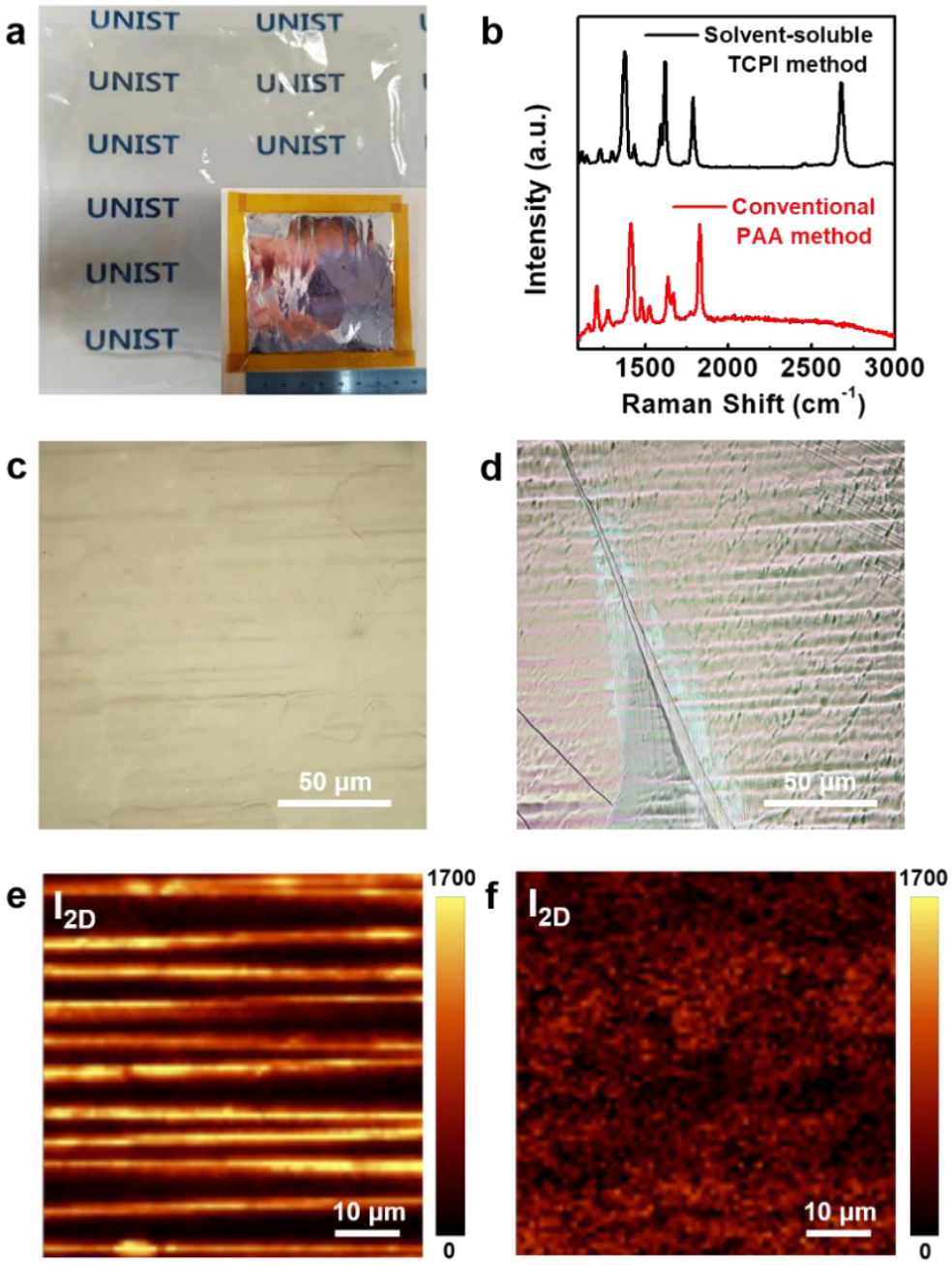

Figure 4.5. TCPI-assisted direct transfer method vs. conventional polymer-assisted wet transfer method for fabrication of TCPI/Gr films. Representative (a, b) OM images, (c, d) Raman spectra, and (e, f) Raman mapping images of graphene 2D peaks of (a, c, e) the transferred TCPI/Gr film using soluble-processable TCPI method and (b, d, f) the TCPI/Gr film on the Cu foil using conventional PAA solution process, respectively.

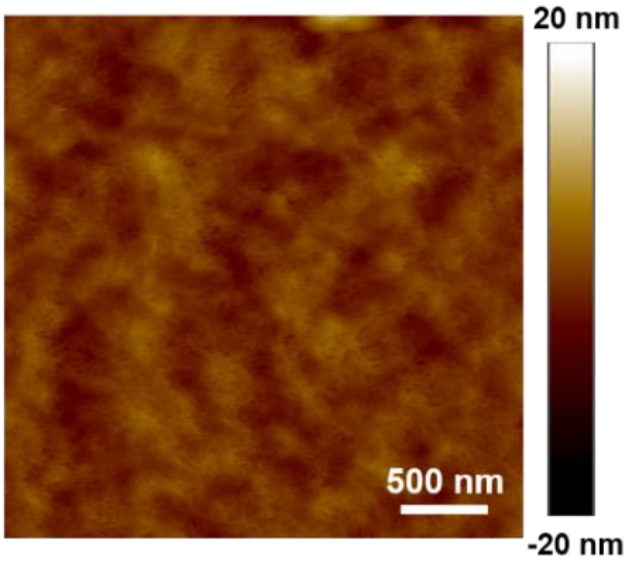

Figure 4.6. Surface morphology of MSA-PDZ/Gr/TCPI hybrid TEs.

4.3.3 Optoelectrical characteristics of TCPI/Gr/acid-treated PDZ

Optoelectrical performance of Gr-based TE structures were analyzed in terms of its functionalization. Due to the trade-off between electrical and optical properties, the transmittance and sheet resistance changes as a function of different numbers of MSA-PDZ coating layers (Figure 4.7). Bare TCPI substrate with thickness of ~40 μm, exhibit 88.6% of high optical transmittance at 550 nm, which is similar to one of 86.4% for commercial PET substrates. After direct transfer of graphene, high optical transparency of graphene lead to a high transmittance of 86.0% at 550 nm for TCPI/Gr films (Figure 2a). In terms of transfer methods, a low sheet resistance of 348 Ω/sq was measured for the high-quality graphene using TCPI transfer method without interfacial perturbation, whereas 460 Ω/sq which is relatively high sheet resistance for PET/Gr fabricated by conventional PMMA method was observed. Depending on the control of PDZ thickness, there was a trade-off between the electrical and optical properties. At the second PDZ layer coating, the Gr/PDZ films exhibit a sheet resistance of 96.37 Ω/sq, with a high transmittance of 80.4% at visible range. Moreover, as an additional functionalization of PDZ, the PDZ film was treated by MSA solution and the functionalization enhanced the electrical conductivity which is twice higher than one of Gr/PDZ films, leading to oxidization and detachment of the insulating PSS region from PEDOT region. Likewise, at the second MSA-PDZ coating, the MSA-PDZ/Gr films could achieve excellent sheet resistance of 48.61 Ω/sq without any reduction in the optical transparency.

Since transparent electrodes experience the tendency of trade-off between optical and electrical properties, there is a widely used evaluation method of the optoelectrical performance, which is Figures of Merit (FoM).[1] The FoM are tools for measuring the performance or effectiveness of device. In the case of transparent electrodes, the FoM indicates the value of direct current (d.c.) conductivity to optical (opt) conductivity (FoM = $\sigma_{d.c.}/\sigma_{opt}$), as follows:

$$\frac{\sigma_{d.c.}}{\sigma_{opt}} = \frac{188.5}{R_s(T_r^{-1/2} - 1)} \quad (3)$$

The minimum requirement for the commercial application is a typical FoM over ~35.[24,77,78] As referring the sheet resistance and transmittance at 550 nm of sample in Figure 4.7 a and b, we can assess the FoM of TEs according to electrode structure and different PDZ thickness. The experimental results can be summarized in Figure 4.7c. In the case TCPI/Gr/PDZ films without acid treatment, the TCPI/Gr without PDZ layer and TCPI/Gr/PDZ films showed good FoM value, which is slightly lower than ~35. After the acid-assisted functionalization of PDZ layers, the FoM value of TCPI/Gr/MSA-PDZ films become twice higher than TCPI/Gr/PDZ films, because the FoM is proportional to electrical conductivity, leading to impressive FoM value of ~70.

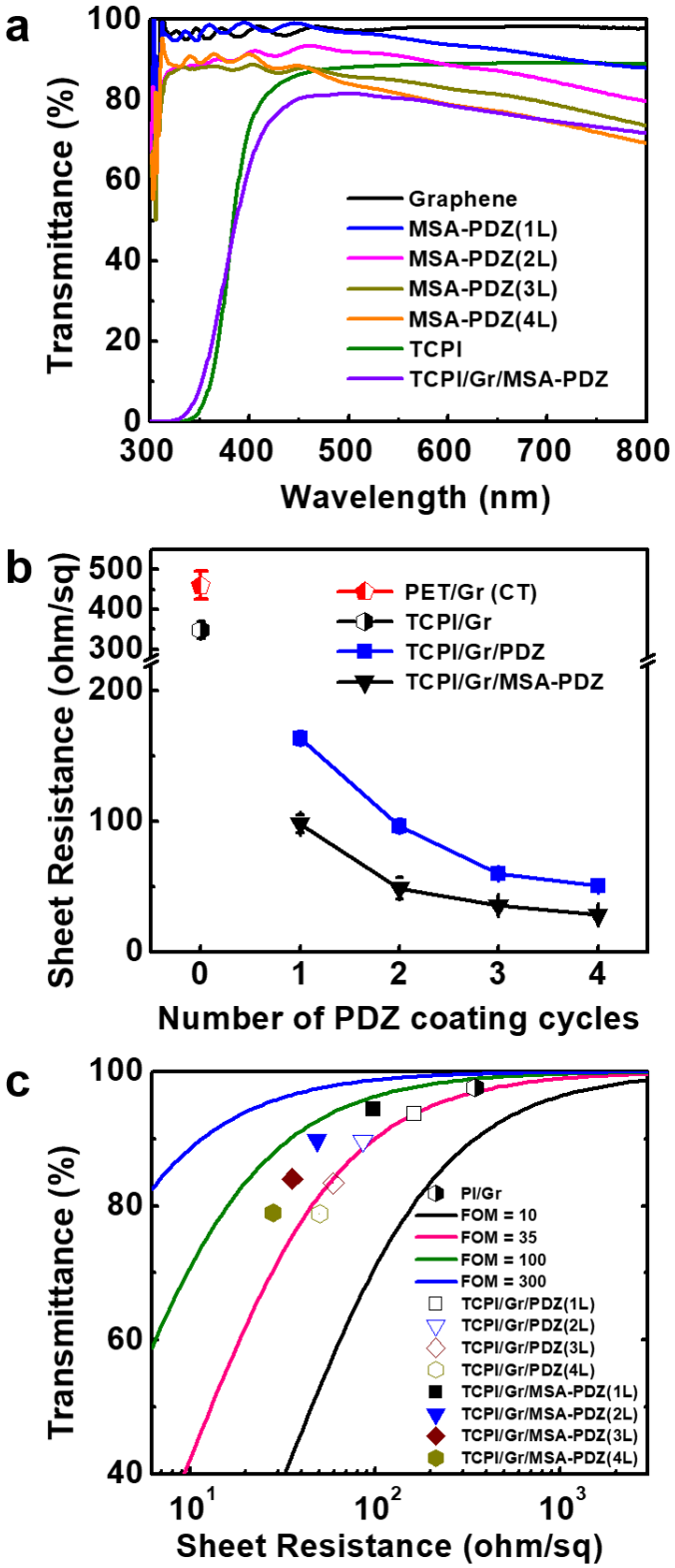

Figure 4.7. Evaluation of optoelectrical characteristics of graphene-based TE films. (a) Optical transmittance range from 300 nm to 800 nm. (b) Electrical properties (sheet resistance) as a function of PDZ coating. (c) Plot for FoM for TEs at 550 nm wavelength.

4.3.4 Environmental stability of TCPI/Gr/acid-treated PDZ

Operational and long-term stabilities is very crucial for For the commercialization of TEs in flexible optoelectronic devices.[9,54,79–87] The inserted graphene layer between TCPI and PDZ layers is expected to improve the mechanical properties and environmental stabilities of the organic TEs, because high-quality monolayer graphene through appropriate fabrication process can act as environmental stable barrier as well as additional effective charge transport path in organic materials.[22,72,88,89] Consecutive bending test with a bending radius of ~1.2 mm was evaluated to confirm its bending stability. In Figure 4.8a, for the TCPI/Gr/MSA-PDZ film, the resistance increases only by ~8 Ω/sq, after 10,000 cycles of bending stress, showing no significant visible cracks or tears. In other words, due to excellent structural characteristics, the TCPI/Gr/ MSA-PDZ films showed excellent endurance under mechanical bending strain.

Thermal stress is another unfavorable factor, which can be easily seen in electronic applications. Moreover, organic materials are fragile to not only heat degradation, but also exposure to water vapor which can be accelerated by heat. In other words, development of heat dissipation layer and gas impermeable barrier is very important for organic optoelectronics.[54,81–87,90] For evaluation of thermal stability, we prepared Gr/MSAPDZ-based electrodes on three different plastic substrates such as TCPI, PET, and parylene. The samples were evaluated as a function of temperature from RT to 350 °C in ambient conditions. In Figure 4.9, in the case of the parylene- and PET-based structure with low glass transition temperature, until 150 °C there is also no degradation in electrical conductivity, but mechanically slightly bent due to their coefficient of thermal expansion. After the temperature approach 150 °C, the electrical conductivity of both sample started to gradually increase. At 260 °C, as soon as temperature approach to decomposition temperature of plastic substrates, both substrates are decomposed. On the other hand, the well-made our TCPI substrates with high glass transition temperature of 243 °C, there is almost no degradation in electrical conductivity to 260 °C. After temperature approaches 260 °C, the resistance of the TCPI/Gr/MSA-PDZ film started to increase gradually. At 350 °C, where one of other plastic substrates cannot endure, our TCPI-based electrodes kept in shape, without decomposition of the TCPI substrates, and the resistance increased by 48%. Above 260 °C, moisture in the air, which was accelerated by surround temperature, may affect the large resistance change of TCPI/Gr/MSA-PDZ.[84–86] or it may be caused by thermal degradation of PEDOT with the decomposition temperature of ~300 °C.[86,87] To analyze the thermal stability in other ways, we implemented TGA analysis. In the case of the PDZ/Gr structure PSS deformation occurs at 280.9 °C, whereas in the case of bare PDZ samples, the decomposition occurred at ~268.6 °C (Figure 4.10). Therefore, we can demonstrate that the intercalated CVD graphene between TCPI and MDS-PDZ films acted as hydrophobic barrier as well as the thermal dissipation layer, improving the thermal

decomposition temperature with high T_g TPCI substrate.

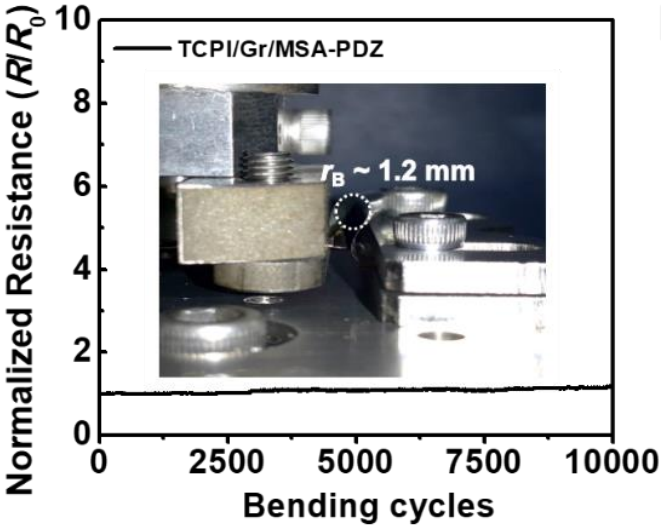

Figure 4.8. Bending stability test for TCPI/Gr/MSA-PDZ at bending radius of 1.2 mm.

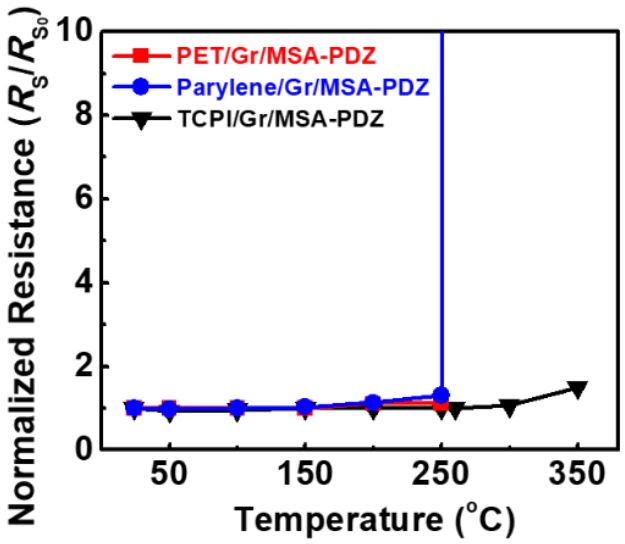

Figure 4.9. Thermal stability tests for TCPI plastics substrates compared to other plastic substrate such as PET and parylene.

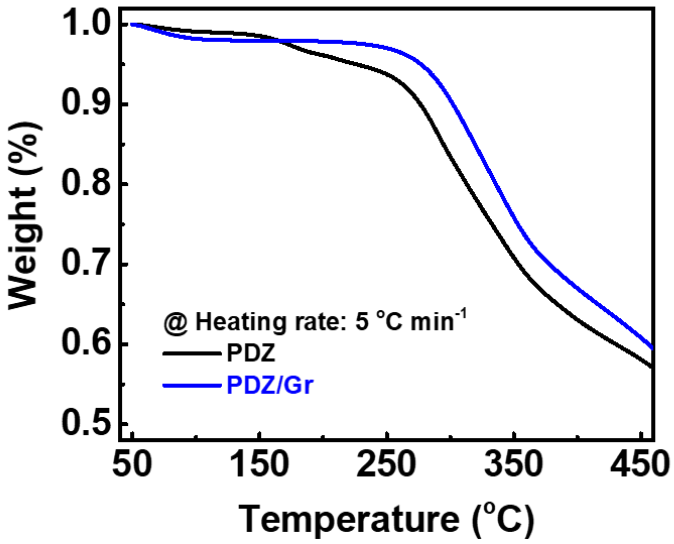

Figure 4.10. TGA analysis of PDZ and PDZ/Gr films in nitrogen atmosphere.

Since organic layers are vulnerable under several environmental conditions and prone to be damaged by moisture, long-term stability under moisture environments is another importance factor for the commercialization of organic optoelectronics. High temperature and high humidity environment accelerate the penetration of vapor and deterioration of organic thin film.[11,79,80,83–85] To prevent the entrance of moisture into the device, hydrophobic TCPI/Gr can acts as gas barrier for organic thin film, so, we implemented comparative analysis in terms of different structures such as bare MSA-PDZ on glass, TCPI/MSA-PDZ without graphene, and TCPI/Gr/MSA-PDZ. There samples were prepared by forming epoxy-coated glasses to block other water penetrating path. Under high temperature over 90 °C and high humidity conditions over 90 %RH, where the penetration of water vapor can be accelerated, the long-term stabilities of prepared samples with different structures were implemented. In Figure 4.11, during 15 days under high temperature conditions (~90 °C), in the case of the bare MSA-PDZ film, the sheet resistance was degraded quickly above 1 kΩ/sq, on the other hand, those of the TCPI/MSA-PDZ increased only to 89.9 and TCPI/Gr/MSA-PDZ samples increased only to 69.4 Ω/sq, showing best endurance. As a results, the TCPI/Gr/MSA-PDZ sample can endure 47.3 and twice times slower than the barrier-free bare PDZ film and graphene-free TCPI/MSA-PDZ, respectively. For high humidity over 90 RH% and T = 50 °C, in the case of TCPI/Gr/MSA-PDZ films, the electrical conductivity decreased only by 2.49 Ω/sq, whereas the bare MSA-PDZ and TCPI/MSA-PDZ films were degraded rapidly, resulting in 15.55 and 8.75 Ω/sq after 24 h, respectively.

For long-term stability test, we implemented multivariate stability test with repetitive multiple factors of thermal stress and humid atmosphere. The multivariate test consisted of repetitive five cycles and one cycle is composed of different environmental conditions: 1st step is 3 h exposure to high temperature (~90 °C), 2nd step is 3 h exposure to room temperature (~25 °C), 3rd step is 3h exposure to low temperature (approximately −50 °C), last, fourth step is exposure to high humidity and high temperature (over 90 RH %, T = 50 °C) at ambient conditions. Due to the assistance of inserted hydrophobic graphene layer, there was almost no change in sheet resistance, exhibiting an increase in sheet resistance only by ~9.7 Ω/sq. On the other hand, in order to evaluate degradation in optical properties, we compared before and after stability tests, in terms of the optical transmittance at 550 nm of visible range. As shown in Figure 4.13, we can confirm that almost no degradation in the transmittance, showing less than 2% at 550 nm of visible range. As a result, we can demonstrate that intercalation of graphene into TCPI/MSA-PDZ layer significantly reinforce the endurance of the organic films in organic optoelectronics under multivariate harsh environments.

Our crucial issue is why operational stability as well as the optoelectronic performance are affected by intercalation of monolayer graphene. First, based on the chemical structures, PEDOT parts of MSA-PDZ and graphene forms strong π−π interaction, leading to a strong doping effect. Moreover, in Chapter

3, we can check graphene can act as an effective path for the charge transfer of PEDOT. From strong interactions, great optoelectrical properties of samples with an FoM of ~70 can be achieved. Second, the gas impermeable and hydrophobic properties of graphene provide shield effects for water vapor by forming potential energy barrier of sp^2 electron clouds, with a periodic electrostatic field (Figure 4.14). Theoretically, the water molecule could not penetrate graphene below 2.86 Å.[8,91,92] Furthermore, development of novel fabrication method using a TCPI solution process make possible direct transfer of large-area high quality monolayer graphene without unnecessary interfacial perturbations. Therefore, the structural characteristics of graphene and MSA-PDZ and novel fabrication method enable the fabrication of graphene-based organic TE structure with excellent optoelectrical properties and operational stabilities while suppressing of water vapor path which can penetrate plastic substrates.

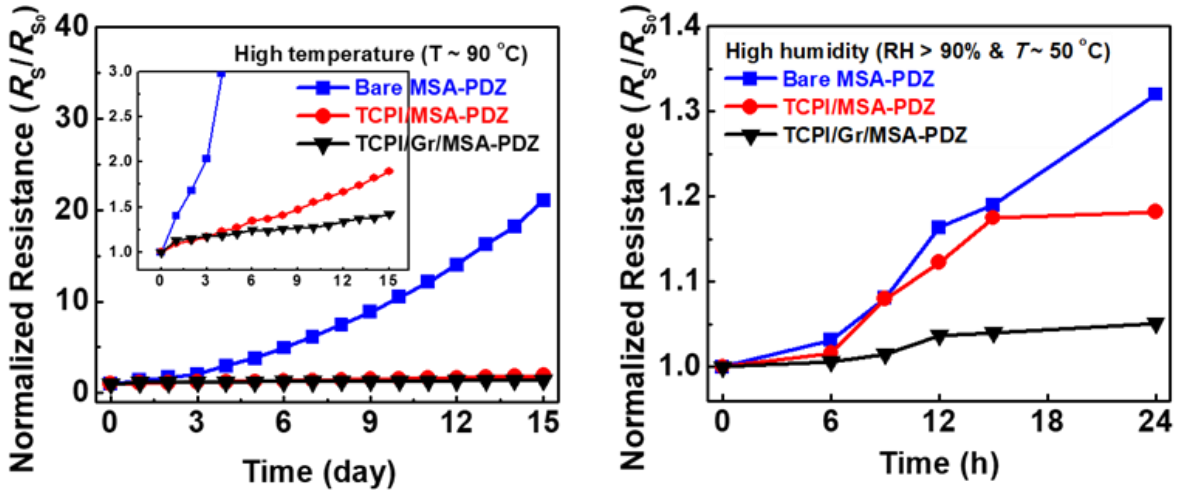

Figure 4.11. Evaluation of operational stabilities of different organic TE structures under temperature of over 90 °C (left) and humidic ambient conditions of RH% > 90% and T = 50 °C (right).

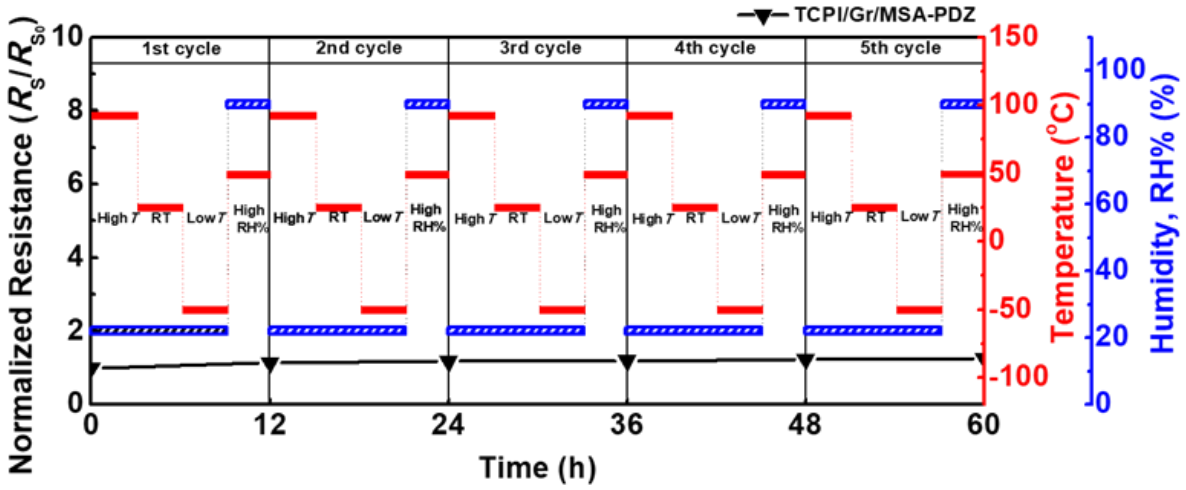

Figure 4.12. Multivariate stability tests for graphene-base TE structure under high & low temperature and humidic ambient conditions.

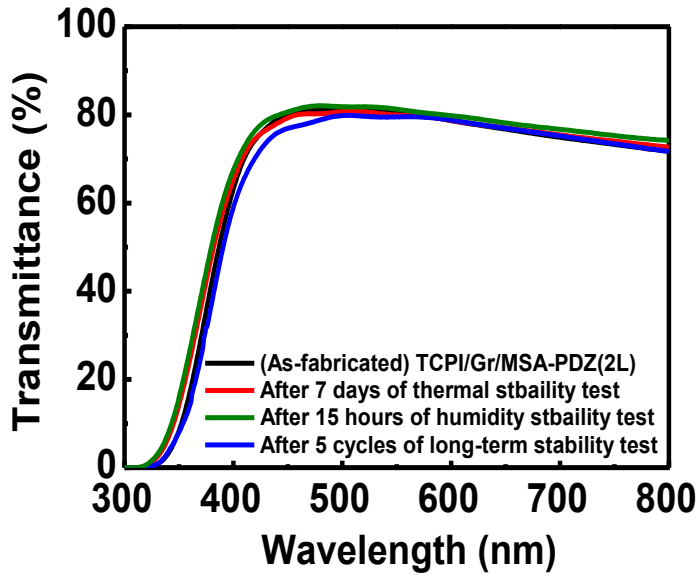

Figure 4.13. Evaluation of change in transmittance of samples before/after diverse stability tests.

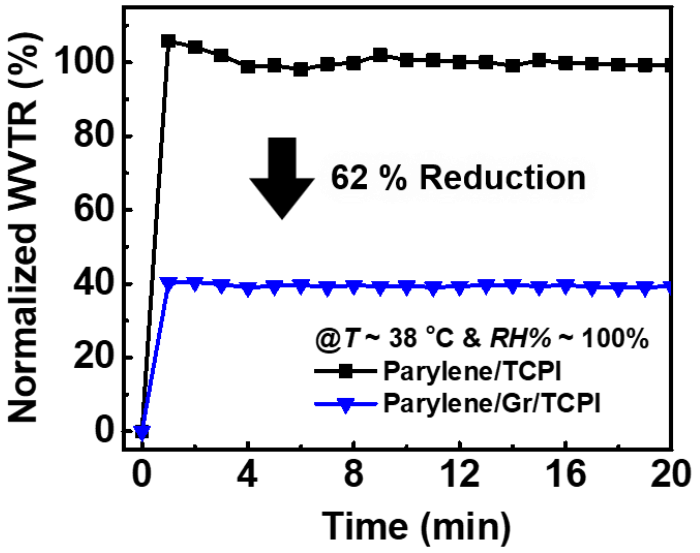

Figure 4.14. Enhanced water vapor barrier properties of the 5-μm-thick parylene-coated TCPI films incorporated with monolayer graphene between the heterostructure.

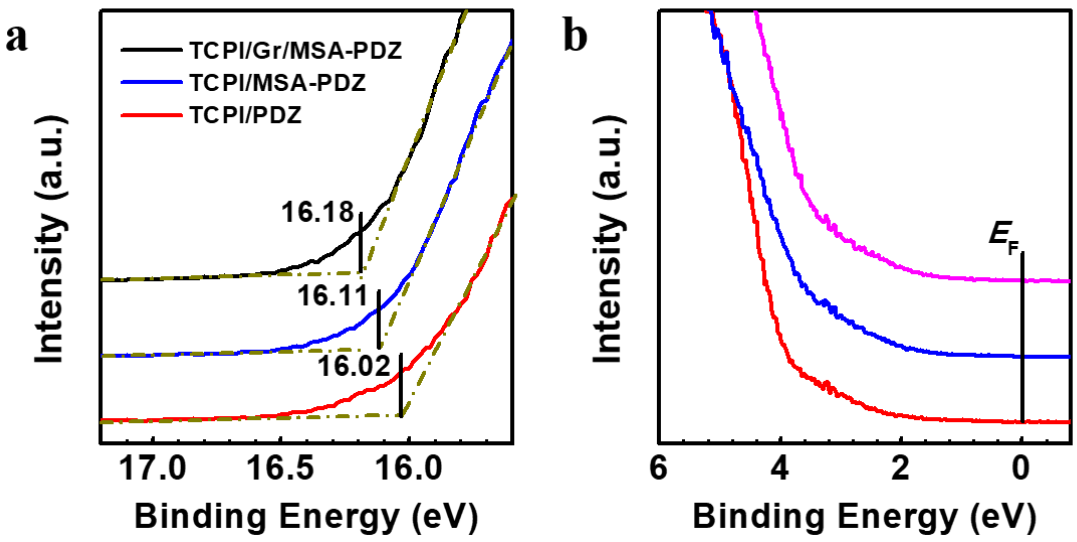

Figure 4.15. (a-b) Ultraviolet photoelectron spectroscopy for the organic thin films.

Structure	E_{Cutoff}	ϕ (eV)
TCPI/PDZ	16.02	5.2
TCPI/MSA-PDZ	16.11	5.11
TCPI/Gr/MSA-PDZ	16.18	5.04
Graphene/PET	16.66	~4.5 eV

Table 4.1. Work functions of bare PDZ, bare MSA-PDZ, Gr-covered MSA-PDZ and pristine CVD graphene.

4.3.5 Application of TCPI/Gr/acid-treated PDZ in PLED

Through the previous studies, we can demonstrate that TCPI/Gr/MSA-PDZ film has a potential viability for practical flexible optoelectronics. As shown in Figure 4.16a, we can successfully apply our sample into PLED devices which is a bottom-emissive type and in order to evaluate the comparative analysis in terms of TE structures, we fabricated four types of PLED devices with different anode structures: glass/ITO, PET/ITO were prepared as reference electrodes and PET/Gr/MSA-PDZ electrode fabricated by PMMA transfer method is prepared to analysis the relevance between interface properties and device performances. Through UPS analysis, we can check TCPI/Gr/MSA-PDZ anode has adequate work function of 5.04 eV for efficient hole injection (Figure 4.15 and Table 4.1). Due to low surface roughness and the clean interface, there is no huge leakage current in the TCPI/Gr/MSA-PDZ-based PLED, which is same with the glass/ ITO-based PLED devices (Figure 4.16b). From the graph slope in Figure 16c, we can estimate the current efficiency. As shown in Figure 4.17, the average device performance in terms of current efficiency and power efficiency for TCPI/Gr/MSA-PDZ-based PLED device can achieve excellent current efficiency of ~15.82 cd/A and power efficiency of ~12.86 lm/W, which is superior to PET/ITO-based PLED (~11.92 cd/A, ~8.14 lm/W) and the glass/ITO-based PLED (~14.05 cd/A, ~11.35 lm/W). Even though the electrical conductivity of TCPI/Gr/MSA-PDZ film is slightly lower than one of Glass/ITO (Table 4.1), the hole injection barrier from the adequate work function (~5.04 eV) of TCPI/Gr/MSA-PDZ is much smaller than ITO of ~4.7 eV.[22,23,35,72] Furthermore, in terms of interface properties, despite the similar anode structure, compared to TCPI/Gr/MSA-PDZ samples, PET/Gr/MSA-PDZ-based PLEDs exhibited high leakage current and poor device performance because of the presence of various interfacial perturbation including PMMA residues, degrading the interface properties and the contact resistance between graphene and MSA-PDZ layers.

Furthermore, we can successfully fabricate TCPI/Gr/MSA-PDZ anode-based flexible PLED devices, as shown in Figure 4.16e, showing uniform luminance without visible degradation at a bending radius of ~2.3 mm. In order to evaluate the flexibility of PLED device, we prepared flexible ITO-based PLED devices for comparative analysis. As shown in Figure 4.16f, unlike PET/ITO-based PLED devices, the PLED device with graphene-based organic TEs can endure the mechanical bending stress over 500 bending cycles at a radius of curvature of ~5 mm, maintaining bright luminance, whereas PET-ITO-based PLEDs lost their light quickly because of its inherent brittleness. In other words, the TCPI/Gr/MSA-PDZ film exhibited great potential for commercial viability in flexible optoelectronics, owing to excellent optoelectrical properties, great operational stabilities and the simple large-area fabrication method.

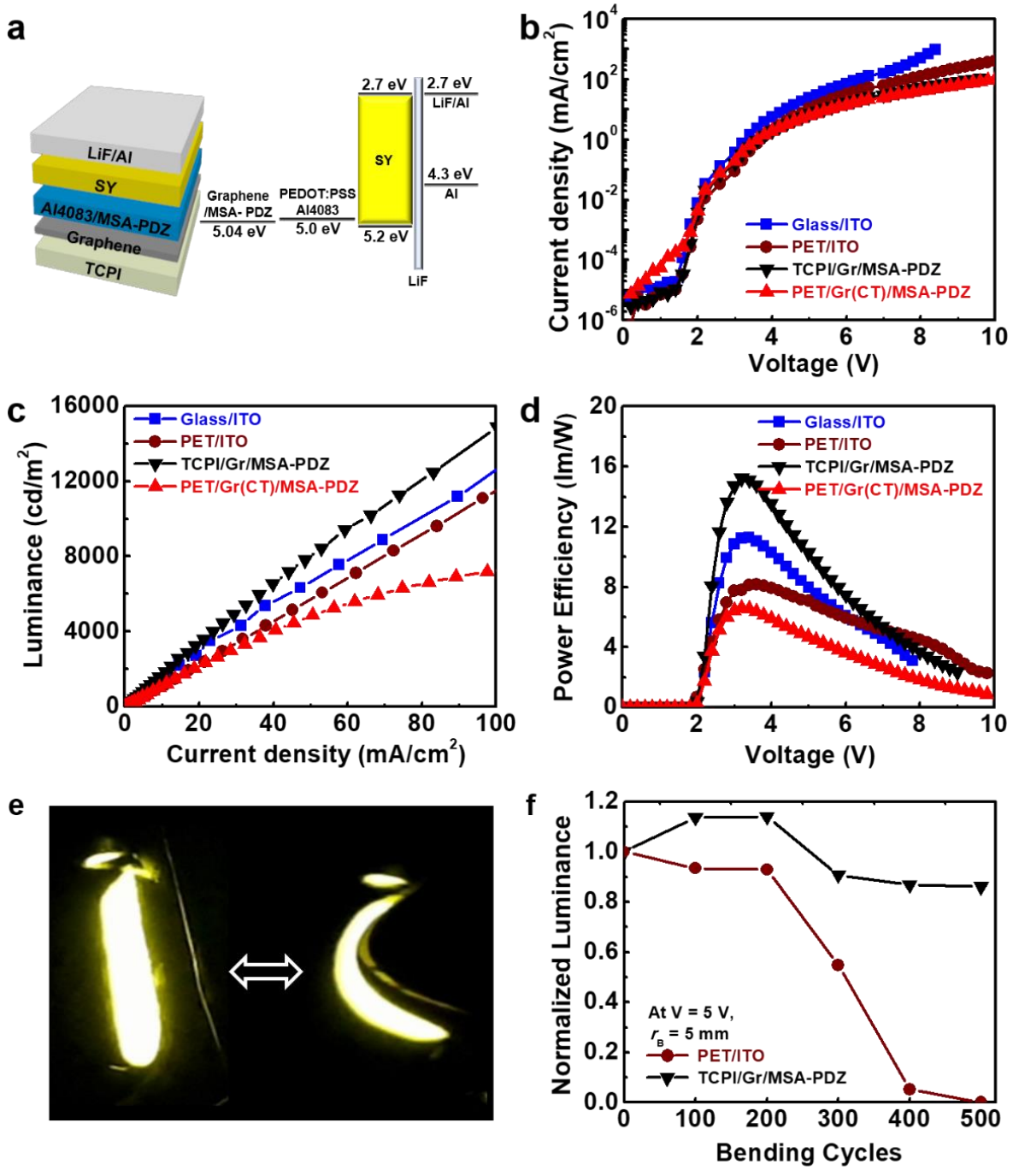

Figure 4.16. PLED performances for four different types of anodes. (a) Schematic of flexible graphene-based TE anode-based PLED and energy level diagram of each components in PLED devices. Changes in (b) current density, (c) current efficiency, (d) power efficiency for four-different PLED devices. (e) Photograph of our flexible PLED at radius of curvature of 2.3 mm. (f) Bending tests for flexible PLED at 5 V, with a radius of curvature of ~5 mm, compared to ITO-based PLEDs.

Table 4.2. Overall Performances of four different types of PLEDs.

Electrode Structure	R_s of Anode [Ω sq^{-1}]	Luminance, max [cd m^{-2}]	CE, max [cd A^{-1}]	PE, max [lm W^{-1}]	EQE, max [%]
Glass/ITO	8	69027 (99,791)	14.05 (16.90)	11.35 (13.84)	4.74 (5.49)
PET/ITO	40	22570 (34941)	11.92 (14.14)	8.14 (9.90)	3.75 (4.30)
TCPI/Gr/MSA-PDZ	48.6	15074 (38351)	15.82 (20.84)	12.86 (22.92)	5.64 (7.25)
PET/Gr(CT)/MSA-PDZ	46.1	5772.7 (8559.1)	8.30 (11.00)	7.10 (9.25)	3.00 (3.97)

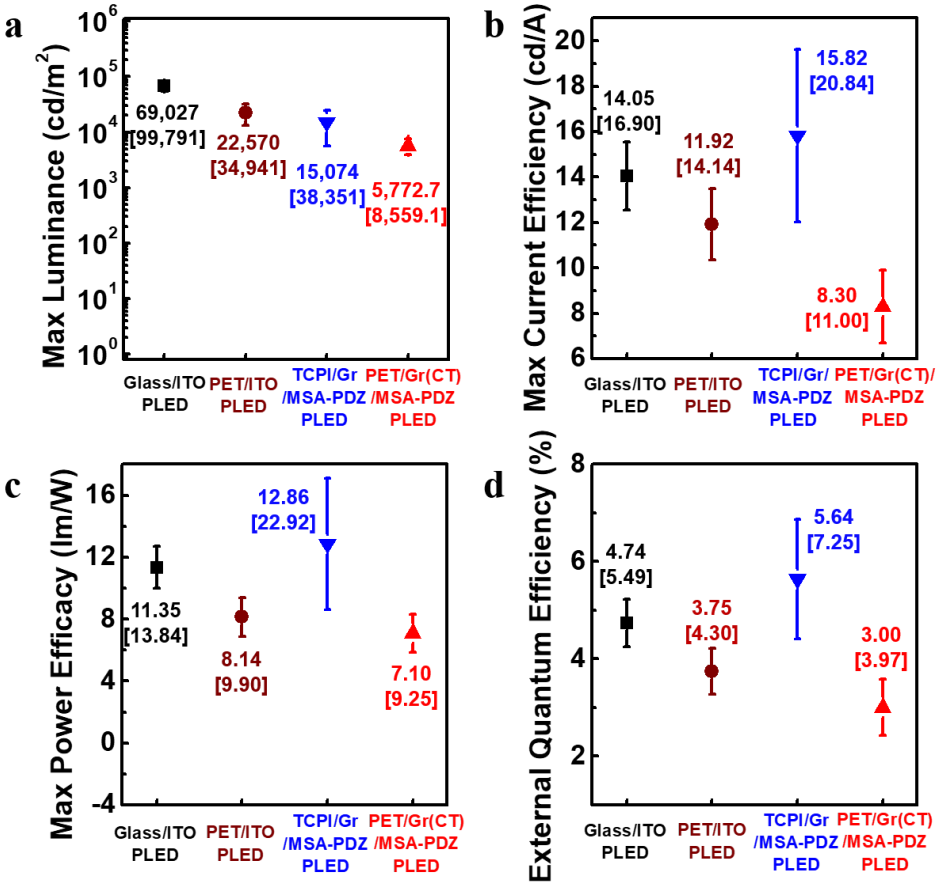

Figure 4.17. Overall device performances of Super Yellow-based PLEDs performances for different types of anode structures, in terms of representative performances: (a)Maximum luminance, (b) maximum current efficiency (CE), (c) maximum power efficiency (PE) and (d) maximum external quantum efficiency (EQE). (The average value is noted as [maximum value of performance].)

4.4 Summary and Outlook

Direct transfer process without unnecessary supporting layer make possible the fabrication of graphene/PDZ TE composite with clean interface on target plastic substrates. In the previous study, we demonstrated that the monolayer CVD graphene can serve as not only an additional charge bypass of PDZ layer but also a barrier for improvement of operational and long-term stabilities of vulnerable organic PDZ layers under unfavorable environmental conditions, exhibiting that the lifetime by thermal degradation increases by two orders.

In this Chapter, we devised simple fabrication process for trilayer graphene-based composite, using solution process of TCPI. We can develop three effects on graphene-based organic TEs, compared to previous study. First, through additional functionalization of PDZ layer, we can enhance electrical conductivity by twice in the same optical transmittance, compared to bare PDZ films. Second, introduction of high-T_g plastic substrate enable our sample to endure over 300 °C. Third, due to solution processability of TCPI, we can devise a new direct transfer method for large-area fabrication, without applying mechanical stress and using unnecessary organic supporting layers. Due to these synergetic effects from trilayer geometry, we can successfully fabricate TCPI/Gr/MSA-PDZ anode-based flexible PLED devices, exhibiting excellent devices performance of a current efficiency and power efficiency of 20.84 cd/A and 22.92 lm/W, respectively. Those efficiencies were superior to those of ITO-based PLEDs. Therefore, we can confirm that this Gr-based organic TE films via novel fabrication method has great potential for commercial viability in of large-scale flexible optoelectronic devices, and we hope that our research work can pave the way for development of optoelectronic devices.

Chapter 5. Conclusion

This dissertation presents fabrication methods of graphene-based organic TE structures for the use in flexible optoelectronic devices. In Chapter 2, we can check the possibility of graphene-based composite for flexible TE, alternative to ITO. Based on this study, we can devise two simple fabrication processes, using lamination process and TCPI solution process. The structural and optoelectrical characteristics of the graphene-based organic TE structures can be further understood in Chapter 3 & 4. The Gr/PDZ fabricated by two fabrication process can achieve excellent optoelectrical performance, because of formation of clean interfaces. In addition, we demonstrated that the monolayer CVD graphene can serve as an effective charge bypass of PDZ layer and a barrier for operational and long-term stabilities under unfavorable environmental conditions, exhibiting that the lifetime by thermal degradation increases by two orders. In Chapter 4, an additional functionalization via acid treatments could result in twice improvement in electrical conductivity of graphene/PDZ films. Based on the optimally functionalized TE structures, we successfully apply our graphene-based TE samples in PLED devices, exhibiting excellent current and power efficiency, superior to ITO-based PLED, in addition to much-enhanced mechanical flexibility. Based on the design of fabrication and characterizations, we can confirm that graphene-based organic TE composites has the great potential in the use of practical optoelectronic applications. In this regard, our results are expected to pave the way for the commercialization of environmental stable and high-performance flexible optoelectronic devices.

Still, there are several works to do for the use of graphene/PDZ TE in practical application. Even though graphene barrier could enhance the operational stabilities of organic materials under various unfavorable conditions, such as thermal stress and exposure to high humidity and ultraviolet light, the polycrystalline monolayer graphene coating onto organic materials actually cannot shield the organic film 100 %, because water molecules are easy to penetrate the grain boundary, tears and void of CVD graphene. Devising new strategies for encapsulation technique such as multilayer stacking and selective deposition on a blank space of graphene will be very interesting field for organic optoelectronic applications. Furthermore, the performance of graphene-based TE structure can be improved by considering other additional treatments on PEDOT:PSS, new fabrication for graphene-based composites with other conducting polymer or metal nanostructure, or geometry of plastic substrates, which can improve stretchability.

References

1. Ellmer, K., Past achievements and future challenges in the development of optically transparent electrodes. *Nat. Photonics* **2012,** *6* (12), 809–817.
2. Zhang, C.; Nicolosi, V., Graphene and MXene-based transparent conductive electrodes and supercapacitors. *Energy Storage Mater.* **2019,** *16*, 102–125.
3. El-Kady, M. F.; Shao, Y.; Kaner, R. B., Graphene for batteries, supercapacitors and beyond. *Nat. Rev. Mater.* **2016,** *1* (7), 16033.
4. Katayama, M., TFT-LCD technology. *Thin Solid Films* **1999,** *341* (1-2), 140–147.
5. Novoselov, K. S.; Geim, A. K.; Morozov, S. V.; Jiang, D.; Zhang, Y.; Dubonos, S. V.; Grigorieva, I. V.; Firsov, A. A., Electric field effect in atomically thin carbon films. *Science* **2004,** *306* (5696), 666–669.
6. Balandin, A. A.; Ghosh, S.; Bao, W.; Calizo, I.; Teweldebrhan, D.; Miao, F.; Lau, C. N., Superior thermal conductivity of single-layer graphene. *Nano Lett.* **2008,** *8* (3), 902–907.
7. Lee, C.; Wei, X.; Kysar, J. W.; Hone, J., Measurement of the elastic properties and intrinsic strength of monolayer graphene. *Science* **2008,** *321* (5887), 385–388.
8. Bunch, J. S.; Verbridge, S. S.; Alden, J. S.; van der Zande, A. M.; Parpia, J. M.; Craighead, H. G.; McEuen, P. L., Impermeable atomic membranes from graphene sheets. *Nano Lett.* **2008,** *8* (8), 2458–2462.
9. Novoselov, K. S.; Fal'ko, V. I.; Colombo, L.; Gellert, P. R.; Schwab, M. G.; Kim, K., A roadmap for graphene. *Nature* **2012,** *490* (7419), 192–200.
10. Li, X.; Cai, W.; An, J.; Kim, S.; Nah, J.; Yang, D.; Piner, R.; Velamakanni, A.; Jung, I.; Tutuc, E.; Banerjee, S. K.; Colombo, L.; Ruoff, R. S., Large-area synthesis of high-quality and uniform graphene films on copper foils. *Science* **2009,** *324* (5932), 1312–1314.
11. Bae, S.; Kim, H.; Lee, Y.; Xu, X.; Park, J. S.; Zheng, Y.; Balakrishnan, J.; Lei, T.; Kim, H. R.; Song, Y. I.; Kim, Y. J.; Kim, K. S.; Ozyilmaz, B.; Ahn, J. H.; Hong, B. H.; Iijima, S., Roll-to-roll production of 30-inch graphene films for transparent electrodes. *Nat. Nanotechnol.* **2010,** *5* (8), 574–578.
12. Berger, C.; Song, Z.; Li, T.; Li, X.; Ogbazghi, A. Y.; Feng, R.; Dai, Z.; Marchenkov, A. N.; Conrad, E. H.; First, P. N.; de Heer, W. A., Ultrathin Epitaxial Graphite: 2D Electron Gas Properties and a Route toward Graphene-based Nanoelectronics. *J. Phys. Chem. B* **2004,** *108* (52), 19912–19916.
13. Ohta, T.; Bostwick, A.; Seyller, T.; Horn, K.; Rotenberg, E., Controlling the electronic structure of bilayer graphene. *Science* **2006,** *313* (5789), 951–954.
14. Kasry, A.; Kuroda, M. A.; Martyna, G. J.; Tulevski, G. S.; Bol, A. A., Chemical doping of large-area stacked graphene films for use as transparent, conducting electrodes. *ACS Nano* **2010,** *4* (7),

3839–3844.

15. Lin, Y. C.; Lu, C. C.; Yeh, C. H.; Jin, C.; Suenaga, K.; Chiu, P. W., Graphene annealing: how clean can it be? *Nano Lett.* **2012,** *12* (1), 414–419.
16. Caldwell, J. D.; Anderson, T. J.; Culbertson, J. C.; Jernigan, G. G.; Hobart, K. D.; Kub, F. J.; Tadjer, M. J.; Tedesco, J. L.; Hite, J. K.; Mastro, M. A.; Myers-Ward, R. L.; Eddy, C. R.; Campbell, P. M.; Gaskill, D. K., Technique for the dry transfer of epitaxial graphene onto arbitrary substrates. *ACS Nano* **2010,** *4* (2), 1108–1114.
17. Kwak, J.; Kim, S. Y.; Jo, Y.; Kim, N. Y.; Kim, S. Y.; Lee, Z.; Kwon, S. Y., Unraveling the Water Impermeability Discrepancy in CVD-Grown Graphene. *Adv. Mater.* **2018,** *30* (30), e1800022.
18. Kim, M.; Shah, A.; Li, C. F.; Mustonen, P.; Susoma, J.; Manoocheri, F.; Riikonen, J.; Lipsanen, H., Direct transfer of wafer-scale graphene films. *2D Mater.* **2017,** *4* (3), 035004.
19. Martins, L. G.; Song, Y.; Zeng, T.; Dresselhaus, M. S.; Kong, J.; Araujo, P. T., Direct transfer of graphene onto flexible substrates. *Proc. Natl. Acad. Sci. U.S.A.* **2013,** *110* (44), 17762–17767.
20. Na, S. R.; Wang, X.; Piner, R. D.; Huang, R.; Willson, C. G.; Liechti, K. M., Cracking of Polycrystalline Graphene on Copper under Tension. *ACS Nano* **2016**, 9616–9625.
21. Kim, K. K.; Reina, A.; Shi, Y.; Park, H.; Li, L. J.; Lee, Y. H.; Kong, J., Enhancing the conductivity of transparent graphene films via doping. *Nanotechnology* **2010,** *21* (28), 285205.
22. Liu, Z.; Li, J.; Sun, Z. H.; Tai, G.; Lau, S. P.; Yan, F., The application of highly doped single-layer graphene as the top electrodes of semitransparent organic solar cells. *ACS Nano* **2012,** *6* (1), 810–818.
23. Lee, B. H.; Lee, J. H.; Kahng, Y. H.; Kim, N.; Kim, Y. J.; Lee, J.; Lee, T.; Lee, K., Graphene-Conducting Polymer Hybrid Transparent Electrodes for Efficient Organic Optoelectronic Devices. *Adv. Funct. Mater.* **2014,** *24* (13), 1847–1856.
24. Kim, Y. H.; Sachse, C.; Machala, M. L.; May, C.; Muller-Meskamp, L.; Leo, K., Highly Conductive PEDOT:PSS Electrode with Optimized Solvent and Thermal Post-Treatment for ITO-Free Organic Solar Cells. *Adv. Funct. Mater.* **2011,** *21* (6), 1076–1081.
25. Yildirim, E.; Wu, G.; Yong, X.; Tan, T. L.; Zhu, Q.; Xu, J.; Ouyang, J.; Wang, J.-S.; Yang, S.-W., A theoretical mechanistic study on electrical conductivity enhancement of DMSO treated PEDOT:PSS. *J. Mater. Chem. C* **2018,** *6* (19), 5122–5131.
26. Xia, Y.; Sun, K.; Ouyang, J., Solution-processed metallic conducting polymer films as transparent electrode of optoelectronic devices. *Adv. Mater.* **2012,** *24* (18), 2436–2440.
27. Rivnay, J.; Inal, S.; Collins, B. A.; Sessolo, M.; Stavrinidou, E.; Strakosas, X.; Tassone, C.; Delongchamp, D. M.; Malliaras, G. G., Structural control of mixed ionic and electronic transport in conducting polymers. *Nat. Commun.* **2016,** *7*, 11287.
28. Jørgensen, M.; Norrman, K.; Krebs, F. C., Stability/degradation of polymer solar cells. *Sol. Energy*

Mater. Sol. Cells **2008,** *92* (7), 686–714.

29. de Jong, M. P.; van Ijzendoorn, L. J.; de Voigt, M. J. A., Stability of the interface between indium-tin-oxide and poly(3,4-ethylenedioxythiophene)/poly(styrenesulfonate) in polymer light-emitting diodes. *Appl. Phys. Lett.* **2000,** *77* (14), 2255–2257.
30. Baranoff, E.; Curchod, B. F.; Frey, J.; Scopelliti, R.; Kessler, F.; Tavernelli, I.; Rothlisberger, U.; Gratzel, M.; Nazeeruddin, M. K., Acid-induced degradation of phosphorescent dopants for OLEDs and its application to the synthesis of tris-heteroleptic iridium(III) bis-cyclometalated complexes. *Inorg. Chem.* **2012,** *51* (1), 215–224.
31. Cameron, J.; Skabara, P. J., The damaging effects of the acidity in PEDOT:PSS on semiconductor device performance and solutions based on non-acidic alternatives. *Mater. Horiz.* **2020**.
32. Lee, M. S.; Lee, K.; Kim, S. Y.; Lee, H.; Park, J.; Choi, K. H.; Kim, H. K.; Kim, D. G.; Lee, D. Y.; Nam, S.; Park, J. U., High-performance, transparent, and stretchable electrodes using graphene-metal nanowire hybrid structures. *Nano Lett.* **2013,** *13* (6), 2814–2821.
33. Rogers, J. A.; Someya, T.; Huang, Y., Materials and mechanics for stretchable electronics. *Science* **2010,** *327* (5973), 1603–1607.
34. An, B. W.; Hyun, B. G.; Kim, S. Y.; Kim, M.; Lee, M. S.; Lee, K.; Koo, J. B.; Chu, H. Y.; Bae, B. S.; Park, J. U., Stretchable and transparent electrodes using hybrid structures of graphene-metal nanotrough networks with high performances and ultimate uniformity. *Nano Lett.* **2014,** *14* (11), 6322–6328.
35. Han, T. H.; Lee, Y.; Choi, M. R.; Woo, S. H.; Bae, S. H.; Hong, B. H.; Ahn, J. H.; Lee, T. W., Extremely efficient flexible organic light-emitting diodes with modified graphene anode. *Nat. Photonics* **2012,** *6* (2), 105–110.
36. Vosgueritchian, M.; Lipomi, D. J.; Bao, Z. A., Highly Conductive and Transparent PEDOT:PSS Films with a Fluorosurfactant for Stretchable and Flexible Transparent Electrodes. *Adv. Funct. Mater.* **2012,** *22* (2), 421–428.
37. Savagatrup, S.; Chan, E.; Renteria-Garcia, S. M.; Printz, A. D.; Zaretski, A. V.; O'Connor, T. F.; Rodriquez, D.; Valle, E.; Lipomi, D. J., Plasticization of PEDOT:PSS by Common Additives for Mechanically Robust Organic Solar Cells and Wearable Sensors. *Adv. Funct. Mater.* **2015,** *25* (3), 427–436.
38. Xia, Y.; Sun, K.; Ouyang, J., Highly conductive poly(3,4-ethylenedioxythiophene):poly(styrene sulfonate) films treated with an amphiphilic fluoro compound as the transparent electrode of polymer solar cells. *Energy Environ. Sci.* **2012,** *5* (1), 5325–5332.
39. Arias, A. C.; MacKenzie, J. D.; McCulloch, I.; Rivnay, J.; Salleo, A., Materials and applications for large area electronics: solution-based approaches. *Chem. Rev.* **2010,** *110* (1), 3–24.
40. Betancur, R.; Romero-Gomez, P.; Martinez-Otero, A.; Elias, X.; Maymó, M.; Martorell, J.,

Transparent polymer solar cells employing a layered light-trapping architecture. *Nat. Photonics* **2013,** *7* (12), 995–1000.

41. Kwak, J.; Chu, J. H.; Choi, J. K.; Park, S. D.; Go, H.; Kim, S. Y.; Park, K.; Kim, S. D.; Kim, Y. W.; Yoon, E.; Kodambaka, S.; Kwon, S. Y., Near room-temperature synthesis of transfer-free graphene films. *Nat. Commun.* **2012,** *3*, 645.
42. D. K. Schroder, *Semiconductor Material and Device Characterization*, John Wiley & Sons, Inc., Third Edition, Hoboken, NJ **2006**.
43. Go, H.; Kwak, J.; Jeon, Y.; Kim, S.-D.; Cheol Lee, B.; Suk Kang, H.; Ko, J.-H.; Kim, N.; Kim, B.-K.; Yoo, J.-W.; Youb Kim, S.; Kim, Y.-W.; Kwon, S.-Y.; Park, K., Low-temperature formation of epitaxial graphene on 6H-SiC induced by continuous electron beam irradiation. *Appl. Phys. Lett.* **2012,** *101* (9) 092105.
44. Reina, A.; Jia, X.; Ho, J.; Nezich, D.; Son, H.; Bulovic, V.; Dresselhaus, M. S.; Kong, J., Large area, few-layer graphene films on arbitrary substrates by chemical vapor deposition. *Nano Lett.* **2009,** *9* (1), 30–35.
45. Nardes, A. M.; Janssen, R. A. J.; Kemerink, M., A Morphological Model for the Solvent-Enhanced Conductivity of PEDOT:PSS Thin Films. *Adv. Funct. Mater.* **2008,** *18* (6), 865–871.
46. Chu, J. H.; Kwak, J.; Kim, S. D.; Lee, M. J.; Kim, J. J.; Park, S. D.; Choi, J. K.; Ryu, G. H.; Park, K.; Kim, S. Y.; Kim, J. H.; Lee, Z.; Kim, Y. W.; Kwon, S. Y., Monolithic graphene oxide sheets with controllable composition. *Nat Commun.* **2014,** *5*, 3383.
47. Ratcliff, E. L.; Bakus Ii, R. C.; Welch, G. C.; van der Poll, T. S.; Garcia, A.; Cowan, S. R.; MacLeod, B. A.; Ginley, D. S.; Bazan, G. C.; Olson, D. C., Formation of interfacial traps upon surface protonation in small molecule solution processed bulk heterojunctions probed by photoelectron spectroscopy. *J. Mater. Chem. C* **2013,** *1* (39).
48. Wang, G. F.; Tao, X. M.; Xin, J. H.; Fei, B., Modification of conductive polymer for polymeric anodes of flexible organic light-emitting diodes. *Nanoscale Res. Lett.* **2009,** *4* (7), 613–617.
49. Wilson, P.; Lekakou, C.; Watts, J., *12th IEEE Conf. Nanotechnology (IEEE-NANO)*, IEEE, Birmingham **2012**.
50. Zabrodskii, A. G.; Zinov'eva, K., *Sov. Phys. JETP* **1984**, 59, 425.
51. Ashizawa, S.; Horikawa, R.; Okuzaki, H., Effects of solvent on carrier transport in poly(3,4-ethylenedioxythiophene)/poly(4-styrenesulfonate). *Synth. Met.* **2005,** *153* (1–3), 5–8.
52. Nardes, A. M.; Kemerink, M.; Janssen, R. A. J.; Bastiaansen, J. A. M.; Kiggen, N. M. M.; Langeveld, B. M. W.; van Breemen, A. J. J. M.; de Kok, M. M., Microscopic Understanding of the Anisotropic Conductivity of PEDOT:PSS Thin Films. *Adv. Mater.* **2007,** *19* (9), 1196–1200.
53. White, M. S.; Kaltenbrunner, M.; Głowacki, E. D.; Gutnichenko, K.; Kettlgruber, G.; Graz, I.; Aazou, S.; Ulbricht, C.; Egbe, D. A. M.; Miron, M. C.; Major, Z.; Scharber, M. C.; Sekitani, T.;

Someya, T.; Bauer, S.; Sariciftci, N. S., Ultrathin, highly flexible and stretchable PLEDs. *Nat. Photonics* **2013,** *7* (10), 811–816.

54. Freirel, M. T. D. A.; Damant, A. P.; Castle, L.; Reyes, F. G. R., Thermal Stability Of Polyethylene Terephthalate (PET): Oligomer Distribution And Formation Of Volatiles. *Packag. Technol. Sci.* **1999,** *12*, 29–36.
55. Horowitz, H. H.; Metzger, G., A New Analysis of Thermogravimetric Traces. *Anal. Chem.* **1963,** *35* (10), 1464–1468.
56. Broido, A., A simple, sensitive graphical method of treating thermogravimetric analysis data. *J. Polym. Sci. A-2 Polym. Phys.* **1969,** *7* (10), 1761–1773.
57. Bom, D.; Andrews, R.; Jacques, D.; Anthony, J.; Chen, B.; Meier, M. S.; Selegue, J. P., Thermogravimetric Analysis of the Oxidation of Multiwalled Carbon Nanotubes: Evidence for the Role of Defect Sites in Carbon Nanotube Chemistry. *Nano Lett.* **2002,** *2* (6), 615–619.
58. Heywang, G.; Jonas, F., Poly(alkylenedioxythiophene)s—new, very stable conducting polymers. *Adv. Mater.* **1992,** *4* (2), 116–118.
59. Yan, Z.; Liu, G.; Khan, J. M.; Balandin, A. A., Graphene quilts for thermal management of high-power GaN transistors. *Nat. Commun.* **2012,** *3*, 827.
60. Flynn, J. H.; Wall, L. A., A quick, direct method for the determination of activation energy from thermogravimetric data. *J. Polym. Sci., Part B* **1966,** *4* (5), 323–328.
61. Densley, R. J.; Salvage, B., Partial Discharges in Gaseous Cavities in Solid Dielectrics under Impulse Voltage Conditions. *IEEE Transactions on Electrical Insulation* **1971,** *EI-6* (2), 54–62.
62. Křižanovský, L.; Mentlík, V., The use of thermal analysis to predict the thermal life of organic electrical insulating materials. *J. Therm. Anal. Calorim.* **1978,** *13* (3), 571–580.
63. Liaw, D. J.; Wang, K. L.; Huang, Y. C.; Lee, K. R.; Lai, J. Y.; Ha, C. S., Advanced polyimide materials: Syntheses, physical properties and applications. *Prog. Polym. Sci.* **2012,** *37* (7), 907–974.
64. Ni, H. J.; Liu, J. G.; Wang, Z. H.; Yang, S. Y., A review on colorless and optically transparent polyimide films: Chemistry, process and engineering applications. *J. Ind. Eng. Chem.* **2015,** *28*, 16–27.
65. Hergenrother, P. M.; Watson, K. A.; Smith, J. G.; Connell, J. W.; Yokota, R., Polyimides from 2,3,3′,4′-biphenyltetracarboxylic dianhydride and aromatic diamines. *Polymer* **2002,** *43* (19), 5077–5093.
66. Thomsen, E.; Muric-Nesic, J.; Everett, V.; Brauers, M.; Davies, E.; Ratcliff, T.; Samundsett, C.; Skryabin, I.; Xia, L.; Blakers, A. In *Materials and manufacturing processes for high-efficiency flexible photovoltaic modules*, 2010 35th IEEE Photovoltaic Specialists Conference, IEEE: 2010; pp 002877–002882.

67. Yeo, H.; Goh, M.; Ku, B.-C.; You, N.-H., Synthesis and characterization of highly-fluorinated colorless polyimides derived from 4,4′-((perfluoro-[1,1′-biphenyl]-4,4′-diyl)bis(oxy))bis(2,6-dimethylaniline) and aromatic dianhydrides. *Polymer* **2015,** *76*, 280–286.
68. Wunderlich, B., *Thermal Analysis*, 1st Ed.; Academic Press: 1990.
69. Foreman, J.; Sauerbrunn, S.; Marcozzi, C., 'Thermal Analysis & Rheology. *Kyoritsu Chem. & Co., Ltd, Kisarazu, Japan* **2013**.
70. Kawakami, H.; Anzai, J.; Nagaoka, S., Gas transport properties of soluble aromatic polyimides with sulfone diamine moieties. *J. Appl. Polym. Sci.* **1995,** *57* (7), 789–795.
71. Deng, B.; Zhang, S.; Liu, C.; Li, W.; Zhang, X.; Wei, H.; Gong, C., Synthesis and properties of soluble aromatic polyimides from novel 4,5-diazafluorene-containing dianhydride. *RSC Adv.* **2018,** *8* (1), 194–205.
72. Chu, J. H.; Lee, D. H.; Jo, J.; Kim, S. Y.; Yoo, J. W.; Kwon, S. Y., Highly Conductive and Environmentally Stable Organic Transparent Electrodes Laminated with Graphene. *Adv. Funct. Mater.* **2016,** *26* (40), 7234–7243.
73. Nevrela, J.; Micjan, M.; Novota, M.; Kovacova, S.; Pavuk, M.; Juhasz, P.; Kovac, J.; Jakabovic, J.; Weis, M., Secondary doping in poly(3,4-ethylenedioxythiophene):Poly(4-styrenesulfonate) thin films. *J. Polym. Sci., Part B: Polym. Phys.* **2015,** *53* (16), 1139–1146.
74. Yang, J.; Lee, M.-H., A water-soluble polyimide precursor: Synthesis and characterization of poly(amic acid) salt. *Macromol. Res.* **2004,** *12* (3), 263–268.
75. Lin, Y. C.; Jin, C.; Lee, J. C.; Jen, S. F.; Suenaga, K.; Chiu, P. W., Clean transfer of graphene for isolation and suspension. *ACS Nano* **2011,** *5* (3), 2362–2368.
76. Zhu, X. Z.; Han, Y. Y.; Liu, Y.; Ruan, K. Q.; Xu, M. F.; Wang, Z. K.; Jie, J. S.; Liao, L. S., The application of single-layer graphene modified with solution-processed TiOx and PEDOT:PSS as a transparent conductive anode in organic light-emitting diodes. *Org. Electron.* **2013,** *14* (12), 3348–3354.
77. Scardaci, V.; Coull, R.; Coleman, J. N., Very thin transparent, conductive carbon nanotube films on flexible substrates. *Appl. Phys. Lett.* **2010,** *97* (2), 023114.
78. Jin, W. Y.; Ginting, R. T.; Ko, K. J.; Kang, J. W., Ultra-Smooth, Fully Solution-Processed Large-Area Transparent Conducting Electrodes for Organic Devices. *Sci. Rep.* **2016,** *6*, 36475.
79. Nardes, A. M.; Kemerink, M.; de Kok, M. M.; Vinken, E.; Maturova, K.; Janssen, R. A. J., Conductivity, work function, and environmental stability of PEDOT : PSS thin films treated with sorbitol. *Org. Electron.* **2008,** *9* (5), 727–734.
80. Giannouli, M.; Drakonakis, V. M.; Savva, A.; Eleftheriou, P.; Florides, G.; Choulis, S. A., Methods for improving the lifetime performance of organic photovoltaics with low-costing encapsulation. *ChemPhysChem* **2015,** *16* (6), 1134–1154.

81. Tyagi, P.; Indu Giri, L.; Tuli, S.; Srivastava, R., Elucidation on Joule heating and its consequences on the performance of organic light emitting diodes. *J. Appl. Phys.* **2014,** *115* (3), 034518.
82. Hsu, J.-M.; Kammer, S.; Jung, E.; Rieth, L.; Normann, R.; Solzbacher, F. In *Characterization of Parylene-C film as an encapsulation material for neural interface devices*, Conference on Multi-Material Micro Manufacture, 2007.
83. Lee, J. J.; Lee, S. H.; Kim, F. S.; Choi, H. H.; Kim, J. H., Simultaneous enhancement of the efficiency and stability of organic solar cells using PEDOT:PSS grafted with a PEGME buffer layer. *Org. Electron.* **2015,** *26*, 191–199.
84. Zhang, H.; Xu, J. K.; Wen, Y. P.; Wang, Z. F.; Zhang, J.; Ding, W. C., Conducting poly(3,4-ethylenedioxythiophene):poly(styrene-sulfonate) film electrode with superior long-term electrode stability in water and synergistically enhanced electrocatalytic ability for application in electrochemical sensors. *Synth. Met.* **2015,** *204*, 39–47.
85. Teng, C.; Lu, X.; Zhu, Y.; Wan, M.; Jiang, L., Polymer in situ embedding for highly flexible, stretchable and water stable PEDOT:PSS composite conductors. *RSC Adv.* **2013,** *3* (20), 7219.
86. Antiohos, D.; Folkes, G.; Sherrell, P.; Ashraf, S.; Wallace, G. G.; Aitchison, P.; Harris, A. T.; Chen, J.; Minett, A. I., Compositional effects of PEDOT-PSS/single walled carbon nanotube films on supercapacitor device performance. *J. Mater. Chem.* **2011,** *21* (40), 15987–15994.
87. Vitoratos, E.; Sakkopoulos, S.; Dalas, E.; Paliatsas, N.; Karageorgopoulos, D.; Petraki, F.; Kennou, S.; Choulis, S. A., Thermal degradation mechanisms of PEDOT:PSS. *Org. Electron.* **2009,** *10* (1), 61–66.
88. Malekpour, H.; Chang, K. H.; Chen, J. C.; Lu, C. Y.; Nika, D. L.; Novoselov, K. S.; Balandin, A. A., Thermal conductivity of graphene laminate. *Nano Lett.* **2014,** *14* (9), 5155–5161.
89. Vadivelu, M. A.; Kumar, C. R.; Joshi, G. M., Polymer composites for thermal management: a review. *Compos. Interfaces* **2016,** *23* (9), 847–872.
90. Na, S. I.; Kim, S. S.; Jo, J.; Kim, D. Y., Efficient and Flexible ITO-Free Organic Solar Cells Using Highly Conductive Polymer Anodes. *Adv. Mater.* **2008,** *20* (21), 4061–4067.
91. Kwak, J.; Jo, Y.; Park, S. D.; Kim, N. Y.; Kim, S. Y.; Shin, H. J.; Lee, Z.; Kim, S. Y.; Kwon, S. Y., Oxidation behavior of graphene-coated copper at intrinsic graphene defects of different origins. *Nat. Commun.* **2017,** *8* (1), 1549.
92. Seethamraju, S.; Kumar, S.; B, K. B.; Madras, G.; Raghavan, S.; Ramamurthy, P. C., Million-Fold Decrease in Polymer Moisture Permeability by a Graphene Monolayer. *ACS Nano* **2016,** *10* (7), 6501–6509.

Academic achievements

Publications:

(1) Song, S.; Sim, Y.; Kim, S.-Y.; Kim, J. H.; Oh, I.; Na, W.; **Lee, D. H.**; Wang, J.; Yan, S.; Liu, Y.; Kwak, J.; Chen, J.-H.; Cheong, H.; Yoo, J.-W.; Lee, Z.; Kwon S.-Y.*, Wafer-scale production of patterned transition metal ditelluride layers for two-dimensional metal-semiconductor contacts at the Schottky-Mott limit, *Nat. Electron.* **2020**, *3*, 207–215.

(2) **Lee, D. H.**‡; Sim Y.‡; Wang, J.; Kwon S.-Y.*, Metal-organic chemical vapor deposition of 2D van der Waals materials - The challenges and the extensive future opportunities, *APL Mater.* (Invited Perspective) **2020**, *8*, 030901.

(3) **Lee, D. H.**; Yun, H. D.; Jung, E. D.; Chu, J. H.; Nam, Y. S.; Song, S.; Seok, S.-H.; Song, M. H.; Kwon, S.-Y.*, Ultrathin graphene intercalation in PEDOT:PSS/colorless polyimide-based transparent electrodes for enhancement of optoelectronic performance and operational stability of organic devices, *ACS Appl. Mater. Interfaces* **2019**, *11*, 21069–21077.

(4) Song, S.; Kim, S.-Y.; Kwak, J.; Jo, Y.; Kim, J. H.; Lee, J. H.; Lee, J.-U; Kim, J. U.; Yun, H. D.; Sim, Y,; **Lee, D. H.**; Seok, S.-H.; Kim, T.-I.; Cheong, H.; Lee, Z.; Kwon, S.-Y.*, Electrically robust single-crystalline WTe_2 nanobelts for nanoscale electrical interconnects, Advanced Science **2019**, *6*, 1801370.

(5) Lim, Y.; Chu, J. H.; **Lee, D. H.**; Kwon, S.-Y.; Shin, H., Increase in graphitization and electrical conductivity of glassy carbon nanowires by rapid thermal annealing, *J. Alloys Compd.* **2017**, *702* (2017), 465–471.

(6) Chu, J. H.; **Lee, D. H.**; Jo, J.; Kim, S. Y.; Yoo, J.-W.;*, Kwon, S.-Y.*, Highly conductive and environmentally stable organic transparent electrodes laminated with graphene, *Adv. Funct. Mater.* **2016**, 26, 7234–7243.

Conference Proceeding:

(1) Highly Conductive Transparent Organic Electrodes Laminated with Graphene Encapsulation for Environmental Stability and Mechanical Properties, Oral presentation, *Materials Research Society of Korea*, Nov 2016. **(Best Presentation Award)**

(2) Graphene-Laminated PEDOT:PSS Films for Highly Conductive, and Environmentally Stable Organic Transparent Electrodes, Poster presentation, *The 24th Korean Conference on Semiconductors*, Feb 2017.

(3) Environmentally Stable and Highly Conductive Graphene-laminated Transparent Electrodes, Poster presentation, *The 10th International Conference on Advanced Materials and Devices*, Dec 2017.

(4) Graphene-laminated organic transparent electrodes with high conductivity and environmental stability, Poster presentation, *The 1st Korean society for LEDs and Optoelectronics*, Feb 2018.

(5) Highly Conductive and Environmentally Stable Graphene-Based Organic Transparent Conducting Film Using Lamination Process, Poster presentation, *The Korean Ceramic Society*, Mar 2018.

(6) Highly Conductive and Environmentally Stable Organic Transparent Conducting Electrode Through Graphene Lamination Process, *The 2nd Korean society for LEDs and Optoelectronics*, Aug 2018.

(7) Insertion of an Ultrathin Graphene Layer in PEDOT:PSS/Colorless Polyimide-Based Transparent Electrodes for Improving the Optoelectronic Performance and Operational Stability of Organic Devices, Poster presentation, *The 4th Korean society for LEDs and Optoelectronics*, Aug 2019.

(8) Ultrathin Graphene Intercalation in PEDOT:PSS/Colorless Polyimide-Based Transparent Electrodes for Enhancement of Optoelectronic Performance and Operational Stability of Organic Devices, Poster presentation, *The 5th International Conference on Advanced Electromaterials*, Nov 2019.

(9) Fabrication of Graphene-Inserted PEDOT:PSS/Colorless Polyimide Composite Flexible Transparent Electrodes, Poster presentation, *The 11th International Conference on Advanced Materials and Devices*, Dec 2019.

(10) Formation of Graphene-Inserted PEDOT:PSS/Colorless Polyimide Composites for High Performance Flexible Transparent Electrodes, Poster presentation, *The 27th Korean Conference on Semiconductors*, Feb 2020.